An evaluation of the Arabian Sea Mini Warm Pool's advancement during its mature phase using a coupled atmosphere-ocean numerical model

Sankar Prasad Lahiri[1], Kumar Ravi Prakash[1,2], Vimlesh Pant[1]

[1]Centre for Atmospheric Sciences, Indian Institute of Technology Delhi, India.

[2]Applied Physics Laboratory, University of Washington Seattle, WA, USA.

Correspondence to: Sankar Prasad Lahiri (sankarprasadlahiri2@gmail.com)

Abstract. A coupled atmosphere-ocean numerical model has been used to examine the relative contributions of atmospheric and oceanic processes in developing the Arabian Sea Mini Warm Pool (MWP). The model simulations were performed for three independent years, 2013, 2016, and 2018, through April-June, and the results were compared against observations. The model simulated sea surface temperature (SST) and sea surface salinity (SSS) bias were less than 1.75ºC and one psu, respectively; this bias was minimal in the MWP region. Moreover, the model simulated results effectively represented the presence of the MWP across the three different years. The mixed layer heat budget analysis indicates that the net surface heat flux raised the mixed layer temperature tendency of the MWP by a maximum of 0.1°C/day during its development phase. The vertical processes exerted a cooling impact on the temperature tendency throughout May and June with a maximum of -0.08ºC/day. Nonetheless, the decrease of net surface heat flux emerges as the dominant factor for the dissipation of the MWP. Further, four sensitivity numerical experiments were performed to investigate the comparative consequences of the ocean and atmosphere on the advancement of the MWP. The sensitivity experiments indicated that pre-April ocean conditions in years with a strong MWP resulted in a 136% increase in MWP intensity in years when MWP SST was close to climatology, which shows the primary role of oceanic preconditioning in determining MWP strength during strong MWP years. Once the oceanic preconditions are met, the atmospheric conditions of weak MWP years lead to an 82% reduction in MWP intensity relative to normal years, highlighting the detrimental impact of atmospheric forcing under such circumstances. Atmospheric conditions, particularly wind, are critical in influencing the spatial evolution and dissipation of MWP in the SEAS by modulating vertical processes. A wind shadow zone, characterized by less turbulent kinetic energy that does not exist during weak MWP years, facilitates the spatial expansion of MWP in SEAS during moderate to strong MWP years.

Formatted ... [1]
Formatted ... [2]
Style Definition ... [26]
Style Definition ... [25]
Style Definition ... [24]
Style Definition ... [23]
Style Definition ... [22]
Style Definition ... [21]
Style Definition ... [20]
Style Definition ... [19]
Style Definition ... [18]
Style Definition ... [17]
Style Definition ... [16]
Style Definition ... [15]
Style Definition ... [14]
Style Definition ... [13]
Style Definition ... [12]
Style Definition ... [11]
Style Definition ... [10]
Style Definition ... [9]
Style Definition ... [8]
Style Definition ... [7]
Style Definition ... [6]
Style Definition ... [5]
Formatted ... [27]
Formatted ... [28]
Formatted ... [29]
Formatted ... [30]
Deleted: K R
Formatted ... [31]
Deleted: ¶ ... [32]
Formatted ... [33]
Deleted: :¶ ... [34]
Formatted ... [35]
Deleted: raises
Formatted ... [36]
Deleted: , thereafter, exert
Formatted ... [37]
Deleted: of -0.08ºC/day in
Deleted: , causing it to dissipate
Formatted ... [38]
Formatted ... [39]
Deleted: indicate…ndicated that pre-April ocean conditio ... [40]
Formatted ... [3]
Formatted ... [4]

1 Introduction

The North Indian Ocean's (NIO) associated ocean-atmosphere dynamics, including monsoon and cyclones, are well explored by researchers. One of the primary determinants in this interconnected process is the sea surface temperature (SST). During the pre-monsoon season, the southern region of the Arabian Sea experienced SST exceeding 28°C, which is associated with the larger Indo-Pacific Warm Pool. However, the highest temperature has been observed in the south-eastern Arabian Sea (SEAS) from late April to May, before the onset of the Indian Summer Monsoon. These patches of warm water in the SEAS are often referred to as the Arabian Sea Mini Warm Pool (MWP) (PV Joseph, 1990; Rao & Sivakumar, 1999; Seetaramayya & Master, 1984; Shenoi et al., 1999). The MWP SST remains 0.5ºC to 1ºC higher than the surroundings during this time. Because the MWP SST stays above 30ºC, well above the minimal criteria for deep convection, it is thought to play a significant role in the Indian Summer Monsoon characteristics over Kerala (Deepa et al., 2007; Masson et al., 2005; Neema et al., 2012; R. R. Rao & Sivakumar, 1999).

Extensive studies have been conducted on the seasonal and interannual evolution of the MWP due to its noteworthy impact on regional climate dynamics (Akhil et al., 2023; Durand et al., 2004, 2007; Kurian & Vinayachandran, 2007; Mathew et al., 2018; Nyadjro et al., 2012; Rao & Sivakumar, 1999; Shenoi et al., 1999). According to Rao and Sivakumar (1999), the East India Coastal Current brings low salinity water to the SEAS in winter, which causes strong stratification and leads to the formation of the MWP in May. Shankar & Shetye (1997) explained the formation of the MWP in terms of the wave propagation phenomenon. The downwelling coastal kelvin wave travels along India's east coast after the summer monsoon has passed, eventually reaching the SEAS in November – December. Later, it is deflected westward by the Rossby Wave, forming the 'Laccadive High' (Bruce et al., 1994, 1998; Shankar & Shetye, 1997). The East India Coastal Current, triggered by the coastal kelvin wave on India's east coast, brings low salinity water to the SEAS and recirculates along the downwelling Laccadive High eddy in November and December. This low salinity water leads to the formation of a barrier layer in the SEAS (Gopalakrishna et al., 2005; Kumar et al., 2009; Masson et al., 2005; Murty et al., 2006; Shenoi et al., 1999). The barrier layer prevents the mixing of water above and below the thermocline (Lukas & Lindstrom, 1991) and traps the incoming shortwave radiation during the pre-monsoon season within the top few meters and thus increases the SST (Hastenrath & Greischar, 1989). Masson et al. (2005) reported that the wintertime barrier layer intensifies the SST of the MWP by approximately 0.5°C.

Kumar et al. (2009) investigated the development of MWP using the Princeton Ocean Model. They stated that salinity has a significant impact on the formation of MWP. Using an ocean general circulation numerical model, Kurian & Vinayachandran (2007) discovered that the orographic influence of the western ghat acts as a wind barrier, increasing net surface heat flux and, hence, MWP intensity. According to Mathew et al. (2018), latent heat flux and incoming shortwave radiation, rather than wintertime freshening, influence the formation of MWP. Recently, Akhil et al. (2023) found that subsurface dynamics during the preceding winter have very little influence on the development of MWP.

Warm water can negatively affect the ocean ecosystem, particularly coral reefs (Abram et al., 2003; Doval & Hansell, 2000; Sarma, 2006). Given its proximity, any sudden increase in the intensity of the MWP could impact biological activity in

Formatted: Font color: Auto

Formatted: Header, Border: Top: (No border), Bottom: (No border), Left: (No border), Right: (No border), Between : (No border), Tab stops: Not at 3.25" + 6.5"

Formatted: Left, Line spacing: single

Deleted: southeastern

Deleted: R. R.

Deleted: R. R.

Deleted: (

Deleted: ,

Formatted: Font color: Auto

Formatted: Footer, Border: Top: (No border), Bottom: (No border), Left: (No border), Right: (No border), Between : (No border), Tab stops: Not at 3.25" + 6.5"

the Laccadive High region. The MWP's impact also affects sound propagation dynamics (Kumar et al., 2007). Despite the evident importance, the formation mechanism of MWP remains a topic of ongoing scientific debate. The complex interplay of factors contributing to the genesis of the MWP, including winter salinity stratification and the presence of the Western Ghats, has been investigated in previous studies (Durand et al., 2004; Gopalakrishna et al., 2005; Kumar et al., 2009; Kurian & Vinayachandran, 2007; Masson et al., 2005; Nyadjro et al., 2012). However, recent findings by Akhil et al. (2023) suggested that the influence of winter salinity stratification on the MWP genesis might be less significant than previously thought. Moreover, a limited number of studies have focused on the air-sea interaction during the mature phase of the MWP, highlighting the need for further research in this area. Kumar et al. (2009) and Mathew et al. (2018) have explored these interactions, but comprehensive analyses remain sparse. Li et al. (2023) recently examined the Arabian Sea warm pool during its mature phase, emphasizing its seasonal and interannual variability using reanalysis datasets. While these studies contribute valuable insights, they primarily address variability over time rather than the specific processes driving the MWP's development and dissipation.

In this study, we examine the impact of the air-sea interaction on the progression of the Arabian Sea Mini Warm Pool using a coupled atmosphere-ocean numerical model. The coupled model employed in this study is calibrated for precise application on a seasonal time scale, which imposes limitations on the duration of simulations. Therefore, long-term simulations in each year are not feasible. Consequently, the present study focuses on configuring a regional coupled atmosphere-ocean numerical model to study the region-specific expansion and dissipation of the MWP. We also aim to elucidate the contribution of oceanic and atmospheric conditions to its growth over the years with distinct MWP intensity. The primary framework of the study is as follows: Section 2 provides an in-depth discussion of the data and methodology, including a detailed explanation of the coupled numerical model. Section 3 demonstrates the results along with the coupled model's ability to simulate temperature, salinity, and currents. Further, a few model sensitivity experiments have been incorporated to explore MWP characteristics and the influence of atmospheric and oceanic conditions across three different MWP events. Section 4 discusses the results and concludes the study with key findings.

2 Data & Methodology

2.1 Data

We utilized the Advanced Very High-Resolution Radiometer (AVHRR) SST dataset, part of the NOAA Climate Data Record program product suite. This dataset combines in-situ and satellite data from 1981 to the present using the optimal interpolation approach and is available on a daily time scale with a spatial resolution of 0.25° (Banzon et al., 2016). In this study, the coupled model's simulated SST is compared with the daily AVHRR SST data for the years 2013, 2016, and 2018. We used weekly SSS data provided by the European Space Agency's Sea Surface Salinity Climate Change Initiative (CCI) to validate the model's simulated sea surface salinity (SSS). This global Level 4 dataset is derived from a multi-sensor combination (SMOS, Aquarius, and SMAP) and spans 2010 to 2020, offering a horizontal resolution of 50 km and a weekly temporal frequency

Formatted: Font color: Auto

Formatted: Header, Border: Top: (No border), Bottom: (No border), Left: (No border), Right: (No border), Between : (No border), Tab stops: Not at 3.25" + 6.5"

Formatted: Font color: Black

Formatted: Font color: Black

Formatted: Font color: Black

Deleted: ¶

Formatted: Font color: Auto

Formatted: Footer, Border: Top: (No border), Bottom: (No border), Left: (No border), Right: (No border), Between : (No border), Tab stops: Not at 3.25" + 6.5"

(Boutin et al., 2021). The model's ability to reproduce ocean surface currents is confirmed using OSCAR surface current data with a horizontal resolution of 0.33° and temporal resolution of 5 days. The numerical model simulated vertical temperature and salinity is compared against AD10 buoy measurement data. AD10 is a moored buoy, and the National Institute of Ocean Technology (NIOT) is entrusted to deploy and collect the moored buoy data, later made available in the Indian National Centre for Ocean Information Services (INCOIS) data portal. The vertical resolution of the buoy data varies with depth.

2.2 Model Details

The coupled atmosphere-ocean numerical model consists of the atmospheric model 'Advanced Research Weather Research and Forecasting' (WRF – ARW) and the ocean model 'Regional Ocean Modeling System' (ROMS). Both models are part of the Coupled Ocean-Atmosphere-Wave-Sediment Transport Modeling System (COAWST) (Warner et al., 2010). The model coupling toolkit (MCT) is used to couple the Atmospheric model WRF-ARW and ocean model ROMS (Jacob et al., 2005). Previously, this coupled numerical model was used to study the air-sea interaction during tropical cyclones (Chakraborty et al., 2022; Prakash et al., 2018; Prakash & Pant, 2017, 2020; Zambon et al., 2014), coastal processes (Carniel et al., 2016; Olabarrieta et al., 2011, 2012; Ricchi et al., 2016; Kumar & Nair, 2015) and monsoon deep depression over the Bay of Bengal (Chakraborty et al., 2023).

The ROMS model is a free-surface, hydrostatic, three-dimensional primitive equations (i.e., Reynolds averaged Navier-Stokes' equation) ocean model widely used in estuarine, coastal, and basin-scale research. The primitive equations in the ROMS model are solved using boundary-fit orthogonal, curvilinear coordinates on a staggered Arakawa C grid (Arakawa & Lamb, 1977). This model employs a terrain-following vertical sigma-coordinate system (Haidvogel et al., 2000; Phillips, 1957; Song & Haidvogel, 1994) and incorporates a variety of advection techniques, such as second and fourth-order center differences and third-order upstream biased method. Vertical mixing in ROMS is handled using either the local Generic Length Scale closure technique (Umlauf & Burchard, 2003) or the nonlocal k-profile boundary layer formulation (Large et al., 1994). Horizontal mixing of momentum and tracers can occur at vertical levels, geopotential, or isopycnal surfaces. Given its very accurate and efficient physical and numerical algorithms, the ROMS model has been widely used to investigate the coastal, open ocean, and biogeochemical processes (Nigam et al., 2018; Paul et al., 2023; Sandeep et al., 2018; Seelanki et al., 2021).

The WRF - ARW atmospheric model is a non-hydrostatic, fully compressible model that predicts mesoscale processes using boundary layer physics schemes and various physical parameterizations (Skamarock & Klemp, 2008; Skamarock, 2008). On a horizontal Arakawa C grid and a vertical sigma-pressure coordinate, WRF - ARW estimates wind momentum components, surface pressure, longwave and shortwave radiative fluxes, dew point, precipitation, surface sensible and latent heat fluxes, relative humidity, and air temperature. WRF is intended to serve and support atmospheric research and operational forecasting needs (Dai et al., 2013). Parameterization schemes are available in microphysics, cumulus parameterization, planetary boundary layer, surface layer, land surface, and longwave and shortwave radiations, with multiple options for each process. In the COAWST modeling system, the WRF code has been modified to provide improved bottom roughness when

Formatted: Font color: Auto
Formatted: Header, Border: Top: (No border), Bottom: (No border), Left: (No border), Right: (No border), Between : (No border), Tab stops: Not at 3.25" + 6.5"
Formatted: Bullets and Numbering
Deleted: Atmosphere-Ocean
Deleted: used in this study
Formatted: Left, Line spacing: single
Deleted: and the model coupling toolkit (MCT)
Deleted: was
Deleted: This
Deleted: . The
Deleted: and microscale
Formatted: Font color: Auto
Formatted: Footer, Border: Top: (No border), Bottom: (No border), Left: (No border), Right: (No border), Between : (No border), Tab stops: Not at 3.25" + 6.5"

computing bottom stress over the ocean (Warner et al., 2010). In addition to WRF and ROMS, the COAWST modelling framework also consists of wave and sediment transport models; however, these components are not used in this study.

2.3 Model Configuration and Experiment Design

The atmospheric component of the coupled numerical model (i.e., WRF model) supports a variety of parameterization schemes. In our WRF configuration we have incorporated the WRF Single-moment-6-class Scheme (Lim & Hong, 2010) as microphysics parameterization to represent grid-scale precipitation processes, the New Tiedtke Scheme for cumulus parameterization that illustrates sub-grid scale convection and cloud detrainment (Zhang & Wang, 2017), the Yonsei University Scheme (Hong et al., 2006) for planetary boundary layer physics, and the MM5 Similarity Scheme (Paulson, 1970). We have used the Unified Noah Land Surface Model (Tewari et al., 2004). At each time step, the atmospheric and land surface models calculate exchange coefficients and surface fluxes of the land or ocean layer and send them to the Yonsei University planetary boundary layer (Hong et al., 2006). The Dudhia Shortwave Scheme (Dudhia, 1989) is used for shortwave radiation parameterization, and the RRTM Scheme (Mlawer et al., 1997) is used for longwave radiation parameterization. The WRF domain has an outer domain resolution of 60 km (18°S to 38°N & 25°E to 95°E) and a nested domain with a 1:3 ratio (Fig. 1). It consists of 40 levels in the vertical direction. WRF is initialized with ERA5 data (Hersbach et al., 2020). The outer domain's lateral boundary condition is taken from ERA5 at 3-hour intervals.

The Ocean model ROMS employed in this study covers the Arabian Sea spanning 10°S - 30°N & 30°E - 85°E with a horizontal resolution of $\frac{1^o}{6}$. A terrain-following sigma coordinate system with 40 vertical levels was used, 20 of which are concentrated in the upper 200 m. The ETOPO2 with 2-minute arc resolution data has been used to create the bathymetry data over the ROMS grid. The surface and bottom stretching parameters for sigma coordinates were set to θ_s=7, & θ_b=1.5, with a critical depth of 10m. The initial conditions and lateral boundary forcings for ROMS were derived from SODAv3.4.2 (Carton et al., 2018) data, having a horizontal resolution of 0.5° × 0.5° with temporal availability of 5-day interval. Momentum and tracer particles were mixed horizontally along the geopotential surface. The non-local K-Profile Parameterization scheme (Large et al., 1994), which integrates the different unresolved processes associated with vertical mixing, was used to deal with the vertical mixing. Horizontal and vertical advection of momentum were treated using third-order upstream and fourth-order centered advection schemes, respectively. The ROMS model employed 60-second baroclinic and 30-second barotropic time steps. Open boundary conditions for momentum and tracers on the southern and eastern boundaries used radiation schemes, allowing remote forcings from the Bay of Bengal and the southern Indian Ocean to influence the domain. Northern and western boundaries were closed. Both the model were initialized from April and simulated till June. A 1-month spin-up period was sufficient to establish the mixed-layer dynamics (the MWP extends till the mixed layer depth (see Fig. S10 in the supplementary)).

Formatted: Font color: Auto
Formatted ... [41]
Deleted: The components
Deleted: the
Formatted: Bullets and Numbering
Deleted: A
Deleted: atmosphere-ocean (WRF+ROMS)
Deleted: was configured over the north Indian Ocean (Fig. 1) to study the influence of oceanic and atmospheric variables in ... [43]
Formatted: Left, Line spacing: single
Deleted:).
Formatted: Font color: Black
Deleted: Longwave
Deleted: ROMS,
Deleted: ocean model, employs several numerical schemes to describe sub-grid processes accurately. Vertical mixing
Deleted: handled by the K-profile parameterization (KPP) mixing scheme (Large
Deleted: 1994).

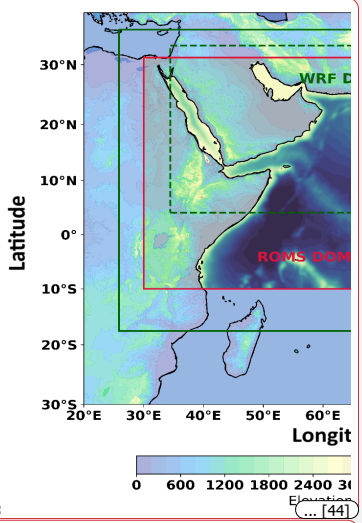

Deleted: ... [44]
Formatted: Font color: Auto
Formatted ... [42]

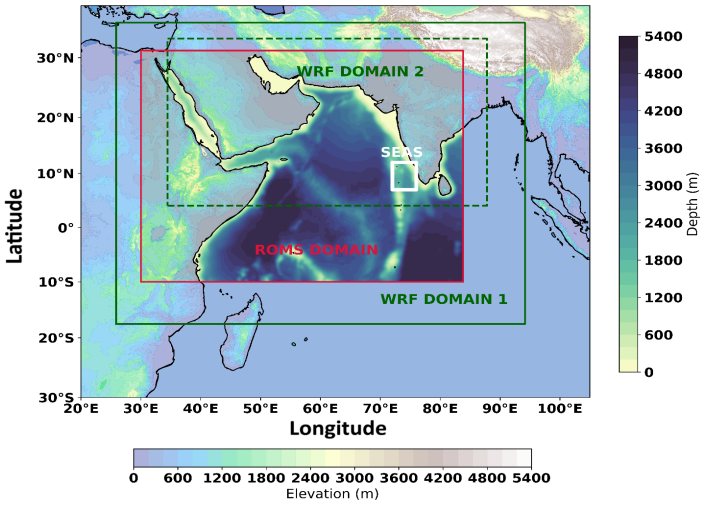

Figure 1: WRF and ROMS model domains. The WRF domain is the green box, while the red box shows the ROMS model domain. Two domains of WRF are shown in solid and dashed green lines. The white box is the south-eastern Arabian Sea (core area of the MWP). Land elevation and ocean Depth are shown in two different contours.

From the previous studies and our own experience (based on our several background experiments), we have observed that the coupled atmosphere-ocean model (part of the COAWST model) would be more accurate when the simulation is up to seasonal scale. Therefore, to assess the MWP using this coupled model, we simulated the model for three independent years (2013, 2016, and 2018), which had distinct MWP characteristics (based on the interannual variation of the MWP area. See Fig. S1 in the supplementary). At every 15 minutes, the WRF and ROMS models interchange variables. While SST is the sole variable that is transferred from ROMS to WRF, other parameters, including 2m air temperature, mean sea level pressure, 10 meters u and v wind velocity, longwave and shortwave radiation, rainfall, and relative humidity are exchanged from WRF to ROMS (readers are referred to Warner et al. 2010 for more details regarding the coupled model). Each run is initialized separately from April 1 to June 20 each year, and the output was saved at daily frequency. The first month of each simulation was used for spin-up and is not included in the analysis. We named this set of runs the control experiment (CNTRL), where we used the SODA and ERA5 data for actual oceanic and atmospheric conditions. Later, to investigate the factors contributing to the evolution of MWP, we designed and performed four idealized numerical experiments using the coupled atmosphere-ocean model with one-way coupling mode. We modified the oceanic and atmospheric conditions in these experiments, as detailed in Table 1. In 2018, the MWP area was closer to climatology (Fig. S1 in supplementary). Hence, this year is used as the base year, and in all four sensitivity experiments, the forcings of the two other years are fed into the 2018 control run.

Formatted: Font color: Auto

Formatted: Header, Border: Top: (No border), Bottom: (No border), Left: (No border), Right: (No border), Between : (No border), Tab stops: Not at 3.25" + 6.5"

Deleted: southeastern

Deleted: The WRF domain has an outer domain resolution of 60 km (18°S to 38°N & 25°E to 95°E) and a nested domain with a 1:3 ratio and consists of 40 levels in the vertical direction. WRF is initialized with ERA5 data. The outer domain's lateral boundary condition is taken from ERA5 at 3-hour intervals. The ROMS model covers the Arabian Sea (10°S - 30°N & 30°E - 85°E) with a horizontal resolution of $\frac{1^{0}}{6}$ and 40 sigma vertical levels, 20 of which are in the top 200 m. The lateral boundary in the ROMS model is closed in the north and west and kept open in the south and east. The preconditioning of oceanic conditions before April is carried into the model through initial and boundary conditions derived from SODA v3.4.2 reanalysis data. ¶
The coupled model is configured in the north Indian Ocean domain, as shown in Fig 1.

Deleted: observe

Deleted: different

Deleted: figure S1).

Deleted: is

Deleted: . ¶

Deleted: outputs we used for analysis in the study are from

Deleted: year's last 50 days of model runs. We leave the remaining outputs for

Deleted: purposes. The variables are exchanged between WRF and ROMS every 15 minutes. Details of the variable exchange between …

Deleted: models are found in Prakash & Pant (2017).

Deleted:). Further

Deleted: have

Deleted: The details of the idealized experiments are shown in Table 1.…

Formatted: Font color: Auto

Formatted: Footer, Border: Top: (No border), Bottom: (No border), Left: (No border), Right: (No border), Between : (No border), Tab stops: Not at 3.25" + 6.5"

Table 1: List of model sensitivity experiments

Experiments Name	Ocean model initial & boundary forcing year	Atmospheric forcing year
Control	2018	2018
$S_{ocean2013}$	2013	2018
$S_{atmos2013}$	2018	2013
$S_{ocean2016}$	2016	2018
$S_{atmos2016}$	2018	2016

2.4 Mixed Layer Heat Budget

The mixed layer heat budget provides a detailed analysis of factors that can contribute to the change in the mixed layer temperature and is calculated using the formula outlined in (Akhil et al. 2023; Foltz & McPhaden 2009; Girishkumar et al. 2017; Nyadjro et al. 2012; Prakash & Pant 2017; Stevenson & Niiler 1983; Vialard et al. 2008) and given as:

$$\frac{\partial T}{\partial t} = \frac{Q_{net}}{\rho C_p h} - \left(u\frac{\partial T}{\partial x} + v\frac{\partial T}{\partial y}\right) + H\left[W_h + \frac{\partial h}{\partial T}\right]\left[\frac{T_h - T}{h}\right] + Residuals \quad (1)$$

Different terms in the above equation's right-hand side (RHS) contribute to temperature tendency differently; the first term on the RHS is the contribution from net surface heat flux; the second is from horizontal advection; and the third is from vertical process and entrainment. T is the average temperature of the mixed layer, t is the time (in days), and h is the mixed layer depth (MLD). In this study, the depth at which the subsurface temperature decreases by 1°C as compared to the surface is used as the isothermal layer depth (ILD) (Kara et al., 2000; Shee et al., 2019; Sprintall & Tomczak, 1992). The MLD is calculated following Shee et al. (2019) as follows.

$$\sigma_{t(z=h)} = \sigma_{t(z=0)} + \Delta T\frac{d\sigma_t}{dt}$$

Where ΔT is the 1°C temperature criteria for ILD, and $\frac{d\sigma_t}{dt}$ is the coefficient of thermal expansion. Meridional and zonal velocity at MLD is given by u, and v. Q_{net} is the net surface heat flux. Here, we have not considered the penetrative shortwave radiation below the MLD. H is the Heaviside step function and is expressed as $H = 0, if \left[W_h + \frac{\partial h}{\partial T}\right] < 0$ or $H = 1, if \left[W_h + \frac{\partial h}{\partial T}\right] > 1$. W_h is the vertical velocity. T_h is the temperature just below (5 m) the depth of the MLD. The residual

Formatted ... [45]
Formatted ... [46]
Formatted ... [49]
Deleted: Experiment Name ... [50]
Deleted: The 2013 ocean initial condition replaces the init ... [52]
Inserted Cells ... [53]
Formatted Table ... [51]
Moved (insertion) [1]
Moved (insertion) [2]
Moved (insertion) [3]
Moved (insertion) [4]
Moved up [3]: 2013
Moved up [1]: 2018
Moved up [2]: 2018
Moved (insertion) [5]
Deleted: The
Deleted: atmospheric forcing replaces the atmospheric fo ... [56]
Deleted: control experiment. The oceanic initial and bour ... [57]
Deleted: .
Inserted Cells ... [58]
Formatted ... [54]
Formatted Table ... [55]
Moved up [4]: 2018
Moved (insertion) [6]
Deleted: The 2016 ocean initial condition replaces the init ... [62]
Inserted Cells ... [60]
Deleted: control experiment. The atmospheric forcing is ... [63]
Moved up [5]: 2018
Deleted: .
Formatted ... [59]
Formatted ... [61]
Moved up [6]: 2018
Moved up [7]: 2018
Moved (insertion) [7]
Deleted: The 2016 atmospheric forcing replaces the atmo ... [65]
Deleted: control experiment. The oceanic initial and bour ... [66]
Deleted: .
Inserted Cells ... [67]
Formatted ... [64]
Formatted ... [68]
Formatted: Bullets and Numbering ... [69]
Formatted ... [70]
Deleted: (…023);… Foltz & McPhaden (…009);… Girish ... [71]
Deleted:);… Nyadjro et al. (…012);… Prakash & Pant ... [72]
Formatted ... [73]
Formatted ... [74]
Formatted ... [75]
Formatted ... [47]
Formatted ... [48]

term represents contributions from other processes, such as diffusion. The units of all the terms here are represented in the $^{o}C.day^{-1}$.

2.5 Potential Turbulent Kinetic Energy (P_{TKE}):

The production of turbulent kinetic energy (P_{TKE}) is used to understand the convective mixing caused by the relative contributions of wind stress (wind-forced momentum flux), freshwater flux (E - P) (haline buoyancy flux), and net surface heat flux (thermal buoyancy flux) (Shankar et al., 2016). P_{TKE} is calculated using the expression given in Han et al. (2001) and Rao et al. (2002) and expressed as:

$$P_{TKE} = \rho u_*^3 + \left[-\frac{\alpha 0.5 g k MLD Q_{net}}{C_p} + 0.5 \rho g k MLD \beta (E - P) S_0\right]$$

Where, $u_* = \sqrt{\frac{\tau}{\rho}}$ is the frictional velocity, τ is the wind stress, ρ is the density of the seawater (1026 $kg.m^{-3}$), k = 0.42 is the Von Kärmän constant, and g is the acceleration due to gravity. E is the evaporation rate, and P is the precipitation. S_0 is the salinity of the ML. Q_{net} is the net surface heat flux. The thermal expansion coefficient (α) and haline contraction coefficient (β) are taken as α = -0.00025 K^{-1} and β = 0.00785 psu^{-1}, respectively, following studies by Shankar et al. (2016) and He et al. (2020). C_p (= 4187 J kg^{-1}) is the ocean's specific heat capacity. The first term on the right-hand side of the above equation represents P_{TKE} due to wind stirring. The first term in the bracket is the P_{TKE} due to thermal buoyancy representing the effect of net surface heat flux, and the second term is P_{TKE} due to the haline buoyancy, which indicates the impact of freshwater change. A negative thermal buoyancy flux implies that heat is lost from the ocean, which causes MLD to deepen. On the other hand, the positive haline buoyancy flux causes more evaporation, which leads to an increase in MLD due to increased salinity (He et al., 2020; Shankar et al., 2016; Shee et al., 2019).

3 Results

3.1 Model Validation:

Figures 2, 3, and 4 compare the coupled model's simulated SST, SSS, and current to observation data in 2018, 2013, and 2016. The mean results and bias are then shown for each of the three years, from May 1 to June 20. The simulated SST effectively captured the cold SST along the Somalia coast across all the examined years, firmly aligning with AVHRR SST data (Fig 2). The SST bias remained within 1°C in all three experiments except in the northern Arabian Sea and along the Somalia coast. In the north Arabian Sea, a cold SST bias and a warm SST bias near the Somalia coast of more than 1°C are observed. In the tropical western Indian Ocean, a cold SST bias was also witnessed in 2013. Despite this, the SST bias remained consistent across the study period, with a minimal bias in the SEAS region (black box in Fig. 2). The model simulated surface salinity revealed a pronounced salinity tongue in the northern Arabian Sea, a feature similarly observed in the ESA salinity data (Fig. 3). The coupled model effectively reproduced the low salinity water in the south-eastern Arabian Sea, with the salinity bias

Formatted: Font color: Auto

Formatted: Header, Border: Top: (No border), Bottom: (No border), Left: (No border), Right: (No border), Between : (No border), Tab stops: Not at 3.25" + 6.5"

Formatted: Bullets and Numbering

Formatted: Left, Line spacing: single

Deleted: dictates

Deleted: indicates

Deleted:).

Deleted: ¶

Deleted: The model simulated SST, sea surface salinity, and surface current were subsequently compared with Advanced Very High-Resolution Radiometer (AVHRR) SST, European Space Agency (ESA) salinity, and Oscar surface current observation data. The spatial resolution of AVHRR, SST, and ESA salinity was 0.25°×0.25°, while the resolution of Oscar current was 0.33°×0.33°. All of these data are of daily temporal resolution. The simulated results from the coupled model were interpolated to the observational resolution before comparing the biases. These comparisons were done for each model simulated year 2018,

Formatted: Left, Line spacing: single

Moved down [8]: 4). Furthermore, the representation of the summer monsoon current in the simulation

Deleted: 2013, and 2016, as shown in Fig. 2, 3 & 4. The mean results and bias are presented for each of the three years, from May 1 to June 20 (Figures 2, 3, and 4). The Indian Ocean is well-known for its seasonally reversing monsoon current. The West India Coastal Current (WICC) transports high salinity water from the northern to southern Arabian Sea in May and June and is the primary driver of inter-basin mass transport (Schott et al., 2009; Schott & McCreary, 2001; Shankar et al., 2002). The model simulated surface currents accurately capture the WICC between May and June for all three years (Fig…

Deleted: is commendable. The simulated SST effectively captures

Deleted: , where a cold bias patch appeared in

Deleted: model simulated SST. This cold bias is attributed to

Deleted: dry anomalous wind originating from

Deleted: northwestern region

Deleted: South Asian landmass, a pattern

Deleted: detected in the CMIP models (S. Sandeep & Ajayamohan, 2014).…

Deleted: remains

Deleted: reveals

Deleted: reproduces

Deleted: southeastern

Formatted: Font color: Auto

Formatted ... [76]

primarily within 0.5 psu across the entire domain, except for a few isolated areas reaching one psu. The Indian Ocean is well-known for its seasonally reversing monsoon current. The West India Coastal Current (WICC) transports high salinity water from the northern to southern Arabian Sea in May and June and is the primary driver of inter-basin mass transport (Schott et al., 2009; Schott & McCreary, 2001; Shankar et al., 2002). The model simulated surface currents accurately captured the WICC between May and June for all three years (Fig. 4). Furthermore, the representation of the summer monsoon current in the simulation was commendable (not shown here).

The coupled model's temperature and salinity profiles were confirmed against buoy measurements at the AD10 location (10.25°N, 72.25°E) (Fig. S2). We utilized the model's nearest point to the AD 10 location to serve this purpose. Before validation, the model-simulated data is interpolated to the vertical resolution of the AD10 buoy data. The AD10 buoy data were available at an hourly time scale from 2012 to 2020 and at a 3-hour frequency in 2021. Except for 2016, the AD10 temperature contains data gaps (Fig. S3 to S5). In 2018, the model temperature had a cold bias below 50m deep at the buoy location. In 2013 and 2016, the model's anticipated temperature had a positive bias of less than 1°C within the top 50 m. Although the vertical temperature is consistent with the AD10 buoy data, the model-simulated salinity data indicates more discrepancies. For instance, in 2018, we found a very high salinity below 50m in AD10, which was not present in our model simulated salinity. Aside from that, the model's represented salinity stayed within one psu bias in 2013 and 2016, with only a few areas exceeding this limit in 2013. The MWP does not extend beyond 50m, and our model-estimated temperature and salinity remain in excellent accord within this depth. To further examine the vertical temperature performance of the model, we conducted a detailed temporal correlation analysis of the simulated temperatures for three distinct control experiments, corresponding to the years 2018, 2013, and 2016. This analysis is performed against observational data obtained from the AD10 buoy location, with calculations made at various depths, specifically at 1, 5, 10, 15, 20, 30, 50, and 100 meters. The results of this statistical assessment are graphically represented in a Taylor diagram (Fig. 5). Across all three control experiments, the standard deviation of the simulated temperature values generally ranged between 0.3 and 1.5, with a few exceptions at certain depths. Additionally, the correlation coefficient between the model simulations and the buoy observations varied from 0.5 to 0.98, indicating a moderate to strong agreement depending on the depth considered.

Formatted: Font color: Auto

Formatted: Header, Border: Top: (No border), Bottom: (No border), Left: (No border), Right: (No border), Between : (No border), Tab stops: Not at 3.25" + 6.5"

Moved (insertion) [8]

Deleted: 1 psu.

Deleted: The vertical temperature and salinity profiles from the coupled model have been validated against buoy measurement at AD10 located at 10.25°N and 72.25°E (Fig S2). The temperature and salinity from the coupled model align well with the AD10 temperature and salinity (Fig. S3 to S5 in supplementary). Additionally, subsurface high salinity water is evident in AD10 and model simulations for 2018, 2013, and 2016.

Deleted: was

Formatted: Font color: Auto

Formatted: Footer, Border: Top: (No border), Bottom: (No border), Left: (No border), Right: (No border), Between : (No border), Tab stops: Not at 3.25" + 6.5"

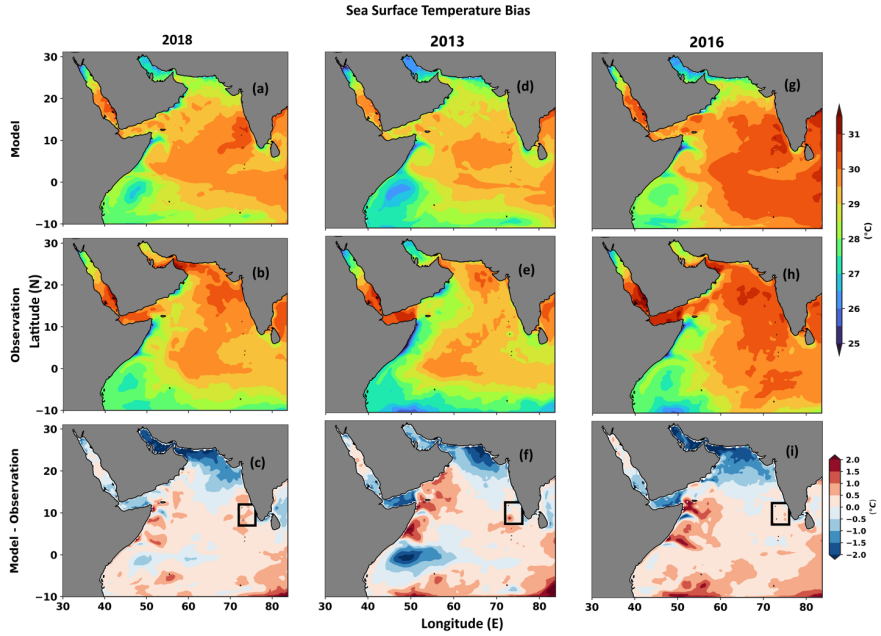

Figure 2: Comparison of model-simulated sea surface temperature (SST) and NOAA-AVHRR surface temperature. Panels (a), (d), and (g) depict model-simulated SST for the years 2018, 2013, and 2016, respectively. Panels (b), (e), and (h) display NOAA-AVHRR SST for the corresponding years. Panels (c), (f), and (i) illustrate the SST difference between model output and observation. The black box delineates the domain of interest overlaid on panels (c), (f), and (i). The mean results and bias are shown for each of the three years, averaged from May 1 to June 20.

Formatted: Font color: Auto

Formatted: Header, Border: Top: (No border), Bottom: (No border), Left: (No border), Right: (No border), Between : (No border), Tab stops: Not at 3.25" + 6.5"

Deleted: Fig. 2

Formatted: Font: Bold

Formatted: Font: Bold

Formatted: Font: Bold

Formatted: Font: Bold

Formatted: Font color: Auto

Formatted: Footer, Border: Top: (No border), Bottom: (No border), Left: (No border), Right: (No border), Between : (No border), Tab stops: Not at 3.25" + 6.5"

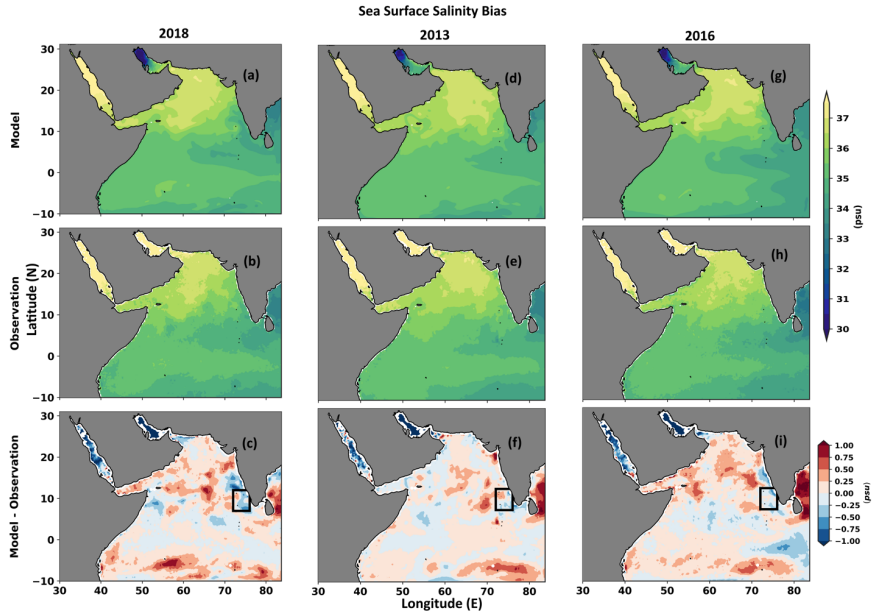

Figure 3: Comparison of model-simulated sea surface salinity (SSS) and ESA-observed SSS. Panels (a), (d), and (g) depict model-simulated SSS for the years 2018, 2013, and 2016, respectively. Panels (b), (e), and (h) display observed SSS for the corresponding years. Panels (c), (f), and (i) illustrate the SSS difference between the model output and observation. The black box delineates the domain of interest overlaid on panels (c), (f), and (i). The mean results and bias are shown for each of the three years, averaged from May 1 to June 20.

Formatted: Font color: Auto

Formatted: Header, Border: Top: (No border), Bottom: (No border), Left: (No border), Right: (No border), Between : (No border), Tab stops: Not at 3.25" + 6.5"

Formatted: Caption, Don't keep with next

Deleted: Fig.

Deleted: 3

Deleted:

Deleted: sea surface salinity.

Formatted: Font: Bold

Deleted:

Formatted: Font: Bold

Formatted: Font: Bold

Formatted: Font: Bold

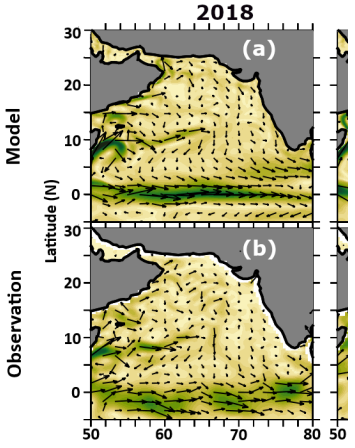

Deleted: Fig. 4

Formatted: Font color: Auto

Formatted: Footer, Border: Top: (No border), Bottom: (No border), Left: (No border), Right: (No border), Between : (No border), Tab stops: Not at 3.25" + 6.5"

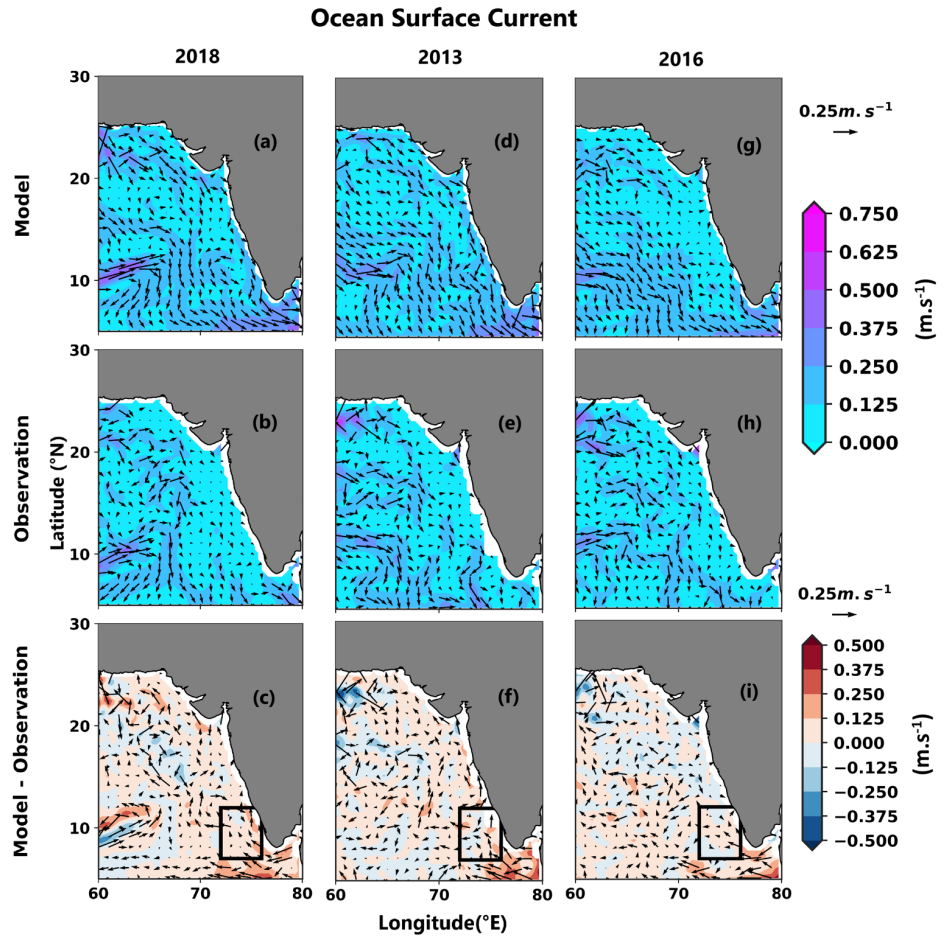

Figure 4: Comparisons of model simulated currents against Oscar surface current. The first column from the left (a-c) is for 2018, the second is for 2013 (d-f), and the last is for 2016 (g to i). As the MWP forms near the western coast of India, the current patterns are shown in the adjacent region, not the whole model domain. Panels (c), (f), and (i) illustrate the difference between the resultant current and the direction between model output and observation. The black box delineates the domain of interest overlaid on panels (c), (f), and (i). The mean results and bias are shown for each of the three years, averaged from May 1 to June 20.

Formatted: Font color: Auto

Formatted: Header, Border: Top: (No border), Bottom: (No border), Left: (No border), Right: (No border), Between : (No border), Tab stops: Not at 3.25" + 6.5"

Deleted: and b

Deleted: c and

Deleted: e and f

Deleted: ,

Deleted: patters

Deleted: for

Deleted: Arabian Sea

Deleted: for

Formatted: Font color: Auto

Formatted: Footer, Border: Top: (No border), Bottom: (No border), Left: (No border), Right: (No border), Between : (No border), Tab stops: Not at 3.25" + 6.5"

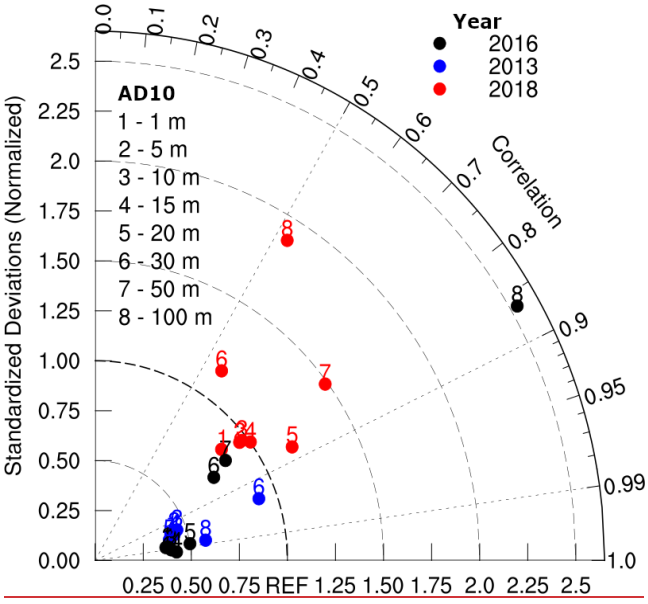

Figure 5: Taylor diagram showing the temporal correlation and standard deviations of model simulated temperature profile from the three years of model experiments with respect to measurements at the buoy AD10; the points at 50 m depth are out of the range of axes for 2013.

3.2 Ocean surface characteristics during various phases of Arabian Sea Mini Warm Pool

Figure 6 shows the model simulated SST, wind stress, and salinity during the mature and dissipation days of MWP. The mature day of the MWP is characterized by the day when SST within the MWP core (shown by the white box in Fig. 1) reaches its highest magnitude in May. The dissipation day is determined when the MWP SST equalizes that of the surrounding water following its mature phase. In addition, the days from the mature to the dissipation are termed the dissipation phase. Previous studies (Li et al., 2023; Rao & Sivakumar, 1999; etc.) have used 30ºC to identify the MWP. A consistent bias of 0.5ºC is

Formatted: Font color: Auto
Formatted ... [77]
Formatted: Caption
Formatted: Font: 10 pt, Not Italic, Font color: Auto
Formatted ... [79]

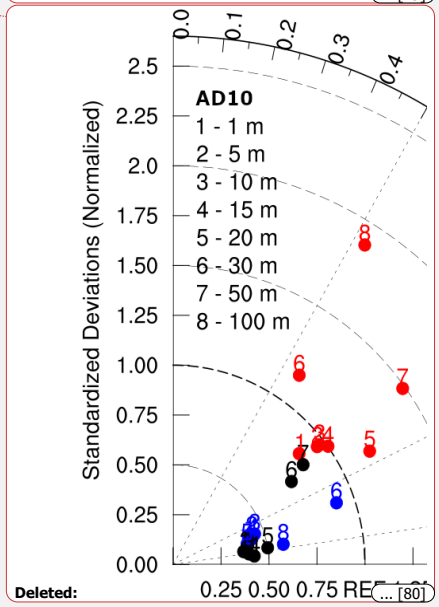

Deleted: ... [80]

Deleted: different
Deleted: ,
Deleted: the year
Deleted: ¶
Deleted: Fig.
Deleted: phases
Formatted: Left, Line spacing: single
Deleted: phase
Deleted: the sea surface temperature (
Deleted:)
Deleted: However, a
Formatted: Font color: Auto
Formatted ... [78]

noticed in SEAS; hence, our study used a threshold of 30.5°C to detect the MWP. In 2018, the SST within the MWP core reached above 31°C on May 20, after which it gradually decreased (Fig. 6a-c). During the mature day in 2018, wind stress over the SEAS was low compared to its surroundings, but wind speed increased considerably afterward. Subsequently, the MWP SST matched the temperature of the surrounding sea by June 8. Despite the absence of the MWP in 2013, the same MWP mature and dissipation day as in 2018 was used for demonstrative purposes (as shown in Fig. 6d-f). In 2016, the MWP matured on May 4 with a larger spatial area than the previous two years (Figs. 6g-i). During the mature day, the wind stress was minimal in the southern Arabian Sea (Fig. 6g). Once the wind stress escalated, the MWP entirely dissipated by June 6, 2016 (Fig. 6h and i).

Table 2: Details of mature and dissipation days in each year with the threshold used to identify the MWP

Year	Mature Day	Dissipation Day	Threshold
2018	May 20	June 8	30.5°C
2013	May 20	June 8	30.5°C
2016	May 4	June 6	30.5°C

Salinity in the vicinity of the MWP was lower during its mature day (<34 psu except in 2013) but increased during its dissipation day (>35.2 psu) (Fig. 7a to 7i). In the MWP core region, salinity was notably less in 2018 compared to the other two years (Fig. 7a). Kumar et al. (2009) reported that low salinity water is one of the reasons behind the MWP development. Yet, in 2016, while the MWP was in its mature stage, low salinity water (less than 34 psu) was detected south of SEAS, slightly outside the core MWP area (Fig. 7g).

Formatted: Font color: Auto

Formatted: Header, Border: Top: (No border), Bottom: (No border), Left: (No border), Right: (No border), Between : (No border), Tab stops: Not at 3.25" + 6.5"

Deleted: Furthermore, in

Deleted: and d

Deleted: phase, the

Deleted: remained less. Following May 20, there is a noticeable rise in

Deleted: stress, and by June 8

Deleted: matches

Deleted: maturity

Deleted: is

Deleted: Figures 6b and 6e

Deleted: extent of the MWP was more substantial

Deleted: in

Deleted: other

Deleted: Fig. 6c & 6f). Furthermore, the MWP was prolonged and matured between May 4 and 7, after which it began to diminish.

Deleted: phase

Deleted: 6c

Deleted: 8.

Formatted: Not Highlight

Deleted: phase

Formatted: Left, Line spacing: single

Deleted: phase

Deleted: 6g to 6i

Deleted: 6i). Additionally, the north Arabian Sea harbors high salinity water (Kumar & Prasad, 1999), which is transported equatorward along the west coast of India through the WICC and reaches the southern tip of India, where it intrudes into the Bay of Bengal (Vinayachandran et al., 2013). The signal of the southeastward propagation of this high salinity water is evident in the sea surface salinity during the mature to dissipation phase of the MWP in all three years (Fig. 6g to 6l).

Formatted: Font color: Auto

Formatted: Footer, Border: Top: (No border), Bottom: (No border), Left: (No border), Right: (No border), Between : (No border), Tab stops: Not at 3.25" + 6.5"

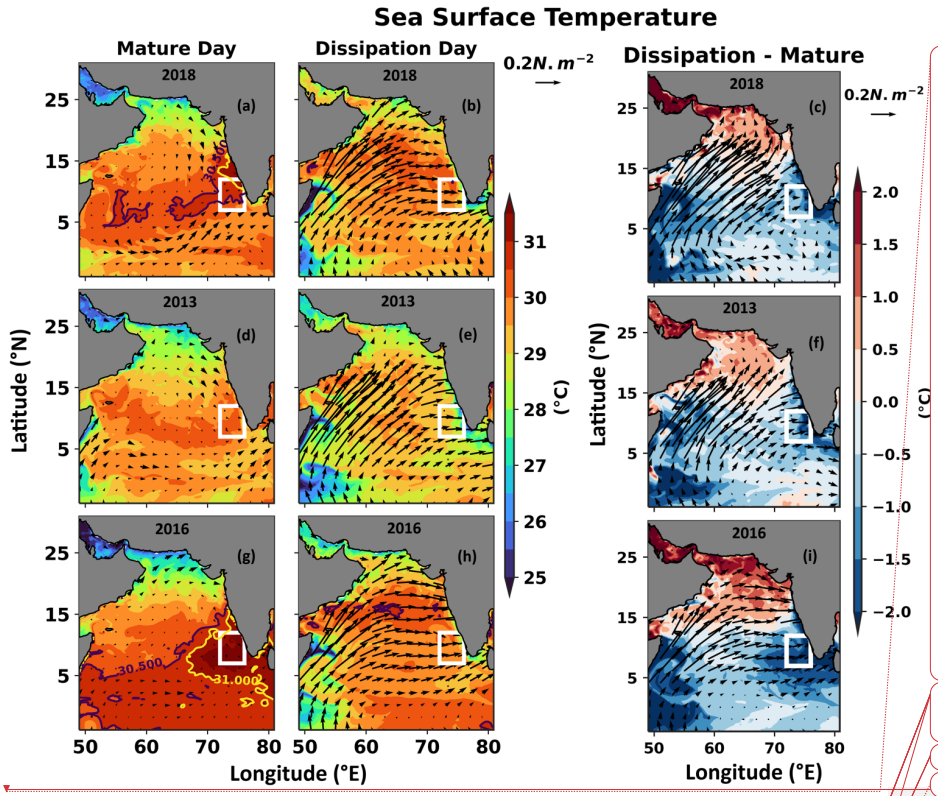

Figure 6: Comparison of SST overlaid by wind stress on mature and dissipation days in 2018 (a-c) (MWP strength close to climatology), 2013 (d-f) (MWP was absent), and 2016 (g-i) (MWP was intense). (c), (f), and (i) show the distinction between dissipation and mature day. The MWP's mature days are May 20, 2018, 2013, and May 4, 2016. The MWP's dissipation days were June 8, 2018, 2013, and June 6, 2016. The black and yellow contours represent 30.5°C and 31°C, respectively. The white box is the core MWP region.

On the mature day of the MWP, there was a positive net surface heat flux across the Arabian Sea except for its southern flank (Fig. 8a, 8d, and 8g). However, as wind stress intensified during the dissipation phase, the net surface heat flux in the Arabian Sea transitioned to negative values in all the years (Fig. 8c, 8f, and 8i). Subsequently, four elements of the net surface heat flux are examined to understand its impact on the regional growth of the MWP in SEAS (Fig. S6 to S9 in supplementary).

Formatted: Font color: Auto

Formatted: Header, Border: Top: (No border), Bottom: (No border), Left: (No border), Right: (No border), Between : (No border), Tab stops: Not at 3.25" + 6.5"

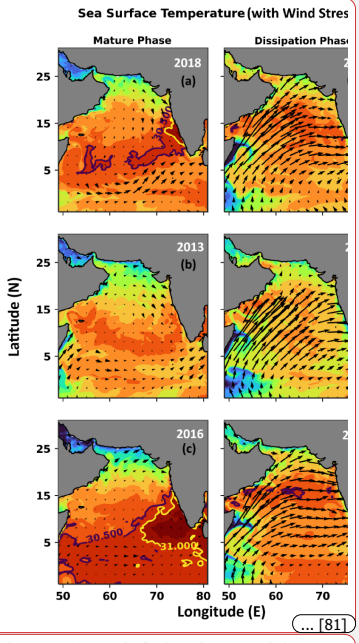

Deleted: ... [81]

Deleted: 6 A comparison… SEQ Figure * ARABIC 6: Comparison of sea surface temperature…ST overlaid by wind stress and salinity during the …n mature and dissipation ... [82]

Formatted ... [83]

Deleted: phase for the mini warm pool is taken on

Deleted: in figures (a) to (f) …epresent the contours of 30.5°C…°C and 31°C ... [84]

Formatted: Font: Bold

Formatted: Font: Bold

Deleted: In

Deleted: phase…ay of the MWP, there was a positive net surface heat flux across the Arabian Sea except for its southern flank (Fig. 7a, 7b…a, 8d, and 7c…g). However, as wind stress intensif ... [85]

Formatted: Left, Line spacing: single

Formatted: Font color: Auto

Formatted: Footer, Border: Top: (No border), Bottom: (No border), Left: (No border), Right: (No border), Between : (No border), Tab stops: Not at 3.25" + 6.5"

The shortwave radiation flux is positive and contributes majorly to the net surface heat flux. Because of the clear sky, the shortwave radiation is higher in April – May (Li et al., 2023). However, once the southwesterly wind strengthens, the subsequent cloudiness blocks the incoming shortwave radiation flux. Consequently, the shortwave radiation flux in the south-eastern Arabian Sea reduced on dissipation day (Fig. S6c, S6f, and S6i in supplementary). The exchange of energy between the atmosphere and ocean is facilitated by turbulent processes, such as sensible and latent heat flux (Large & Pond, 1981). As the wind speed increases, the loss of the latent heat flux increases from the mature to the dissipation day in all the years (Fig. S8c, S8f, and S8i in supplementary).

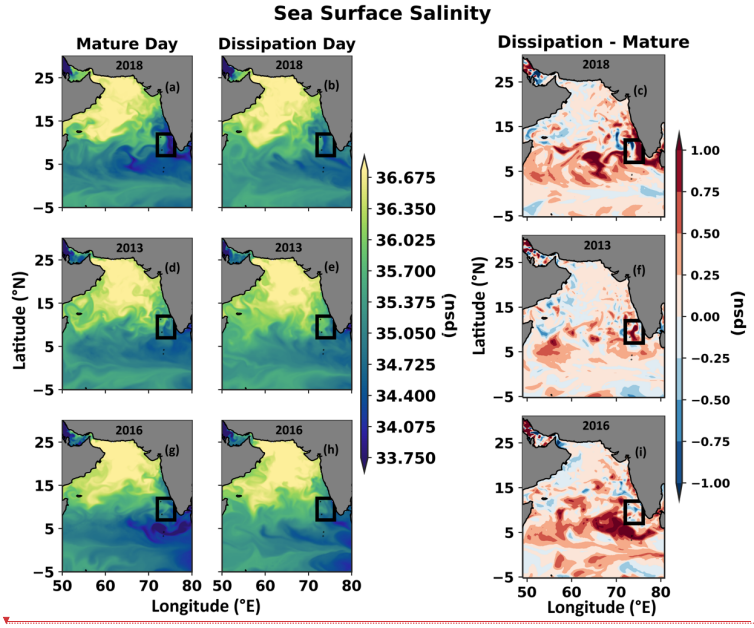

Figure 7: Comparison of sea surface salinity on mature and dissipation days in 2018 (a-c) (MWP strength close to climatology), 2013 (d-f) (MWP was absent), and 2016 (g-i) (MWP was intense). (c), (f), and (i) show the distinction between dissipation and mature day. The MWP's mature days are May 20, 2018, 2013, and May 4, 2016. The MWP's dissipation days were June 8, 2018, 2013, and June 6, 2016. The black box is the core MWP region.

Formatted: Font color: Auto

Formatted: Header, Border: Top: (No border), Bottom: (No border), Left: (No border), Right: (No border), Between : (No border), Tab stops: Not at 3.25" + 6.5"

Deleted: always

Deleted: Longwave

Deleted: was negative

Deleted: S6

Deleted: However, these components of the net heat flux can't justify the progress of the MWP in the SEAS.

Deleted: ¶ ... [87]

Deleted: 7 Same as Fig. 6 but for net heat flux during the

Deleted: day of the MWP

Deleted: ,

Formatted: Caption, Left, Line spacing: single

Deleted: ,

Deleted: .¶ ... [88]

Deleted: core area (white box in Fig 1). In 2018 and 2016, the high-temperature water associated with the MWP extended ... [89]

Deleted: more prolonged in 2016 without any break (Fig 8c). The mixed layer heat budget in the core region of the MWP (72- ... [90]

Deleted: .¶ ¶ ... [91]

Deleted: panels (c) and (f) are for

Deleted: red dashed line suggests the zero line.¶ ¶ ... [92]

Deleted: of the MWP. For instance, since May 23, 2018, SEAS witnessed a remarkable decline in mixed layer temperat ... [93]

Formatted: Font color: Auto

Formatted ... [86]

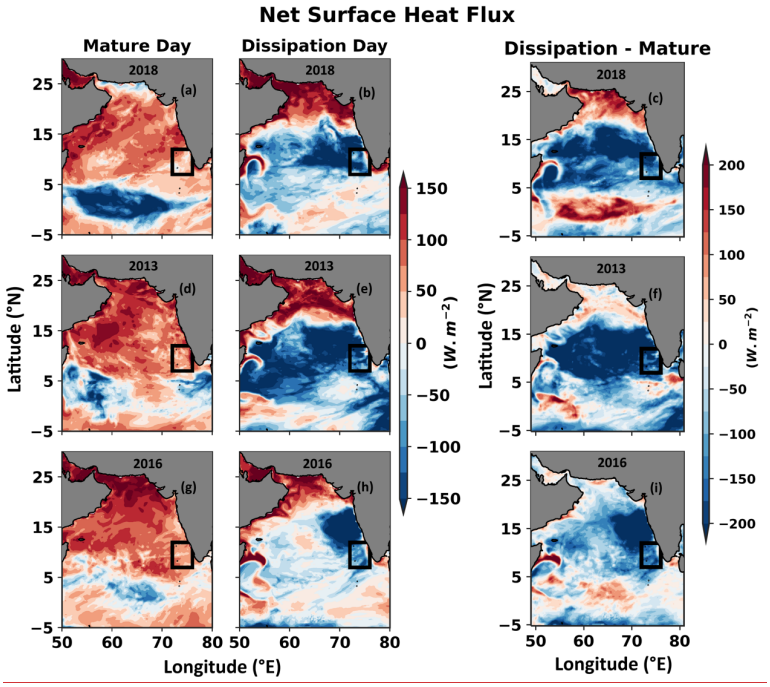

Figure 8: Same as Fig. 7 but for net surface heat flux.

3.3 Causative Factors

3.3.1 The Role of the Atmosphere and Ocean in the Formation of MWP

This section examines the relative contributions of the ocean and atmosphere to the development of the MWP through four sensitivity experiments (see Table 1 for details). In the $S_{ocean2013}$ and $S_{ocean2016}$ experiments, the ocean initial and boundary conditions from 2013 and 2016 replace those in the 2018 control experiment, respectively. The MWP remains very strong (weak) in the $S_{ocean2016}$ ($S_{ocean2013}$) experiment and reaches its maximum extent on May 20 (Fig. 9a and b is compared with 9c). An intense MWP was developed in the 2016 control experiment, and a similar MWP is also seen in $S_{ocean2016}$. The initial mean pre-April ocean temperature in SEAS (initial condition temperature is averaged within the white box in Fig. 9 and 10 and till the MLD) was 0.35°C higher in 2016 (0.15°C lower in 2013) compared to 2018. Following the initial conditions, the MWP core temperature within the MLD was 0.6°C higher in $S_{ocean2016}$ (0.3°C lower in $S_{ocean2013}$) compared to the 2018 control

Formatted: Font color: Auto

Formatted: Header, Border: Top: (No border), Bottom: (No border), Left: (No border), Right: (No border), Between : (No border), Tab stops: Not at 3.25" + 6.5"

Formatted: Bullets and Numbering

Formatted: Left, Line spacing: single

Deleted: the

Deleted: didn't form; however,

Deleted: reveals the presence of a weak

Deleted: near the coast in the SEAS (Fig 9). In contrast,

Deleted: experienced anomalously warm conditions, with the

Deleted: SST exceeding 31°C at its core (Fig 6c). Similarly, the MWP core SST reaches a maximum temperature exceeding 31°C in the $S_{ocean2016}$ experiment (Fig 9). In the MWP core, the initial

Deleted: 15°C lower in 2013 and 0.

Deleted: is 0.3°C lower in $S_{ocean2013}$ and

Formatted: Font color: Auto

Formatted: Footer, Border: Top: (No border), Bottom: (No border), Left: (No border), Right: (No border), Between : (No border), Tab stops: Not at 3.25" + 6.5"

simulation during the mature day (Fig. S10d and S10e are compared with Fig. S10a in the supplementary). These results indicate that the pre-April ocean conditions strongly influence the intensity of the MWP.

Later, in the $S_{atmos2013}$ experiment, the 2013 atmospheric conditions were replaced with the same in the 2018 control experiment. MWP is absent in the 2013 control and $S_{atmos2013}$ experiments (Fig. 10a and 6d). Similarly, the 2016 atmospheric conditions replace those used in the 2018 control experiment, which is termed the $S_{atmos2016}$ experiment. A strong MWP was observed in the $S_{atmos2016}$ experiment (Fig. 10b), albeit with a lower intensity than in the 2016 control (Fig. 6g) and $S_{ocean2016}$ (Fig. 9b) experiment, indicating that pre-April ocean conditions were responsible for the formation of an intense MWP in the 2016 control experiment. In the $S_{atmos2016}$ and 2016 control experiments, the MWP matured on May 4. Similarly, the $S_{ocean2016}$ and 2018 control experiments have analogous atmospheric conditions, and the MWP matures on May 20 (Fig. 9b and 9c). These findings suggest that the atmospheric variables determine the spatial variability of the MWP as well as the day of maturation.

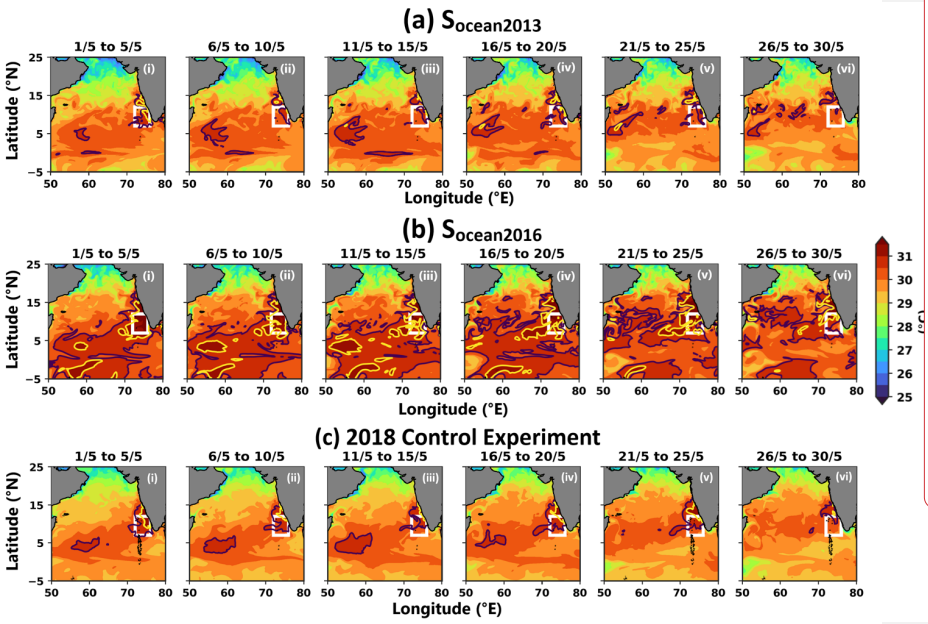

Figure 9: 5-day average evolution of SST from May 1 to May 30 for the experiment (a) $S_{ocean2013}$, (b) $S_{ocean2016}$, and (c) 2018 control experiment. In these two experiments, the ocean's initial condition was replaced in 2013 and 2016 in the 2018 control experiment. See Table 1 for further details about the experiments. The black and yellow contours

Formatted: Font color: Auto

Formatted: Header, Border: Top: (No border), Bottom: (No border), Left: (No border), Right: (No border), Between : (No border), Tab stops: Not at 3.25" + 6.5"

Deleted: throughout

Deleted: phase

Deleted: S7a

Deleted: S7c

Deleted: 8a). These differences in the temperature solely correspond to the ocean's initial condition before April.

Deleted: In the $S_{atmos2013}$ experiment, no sign of the MWP is noticed (Fig. 10). Further, in the $S_{atmos2016}$ experiment, the MWP matures from the 1st to the 8th of May (Fig 10). However, the MWP reached its mature condition in the 2018 control experiment on May 20. Additionally, in the $S_{atmos2016}$ experiment, the MWP became very weak in its area and magnitude on May 20, indicating the influence of the prevailing atmospheric conditions on modulating the MWP's spatial variability. ¶

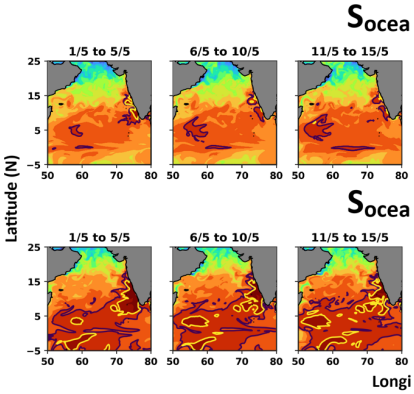

Fig. 9 5-day average Evolution of SST from May 1 to May 30 for the experiment $S_{ocean2013}$ and $S_{ocean2016}$. In these two experiments, the ocean's initial condition was changed to 2013 and 2016 in the 2018 control experiment. See Table 1 for further details. The black contour denotes a 30.5°C contour while the yellow contour represents a 31°C contour. The days associated with mean evolution are displayed at the top of each subplot.¶ ... [94]

Formatted: Font color: Auto

Formatted: Footer, Border: Top: (No border), Bottom: (No border), Left: (No border), Right: (No border), Between : (No border), Tab stops: Not at 3.25" + 6.5"

represent 30.5°C and 31°C, respectively. The days associated with mean evolution are displayed at the top of each subplot. The white box is the core MWP region.

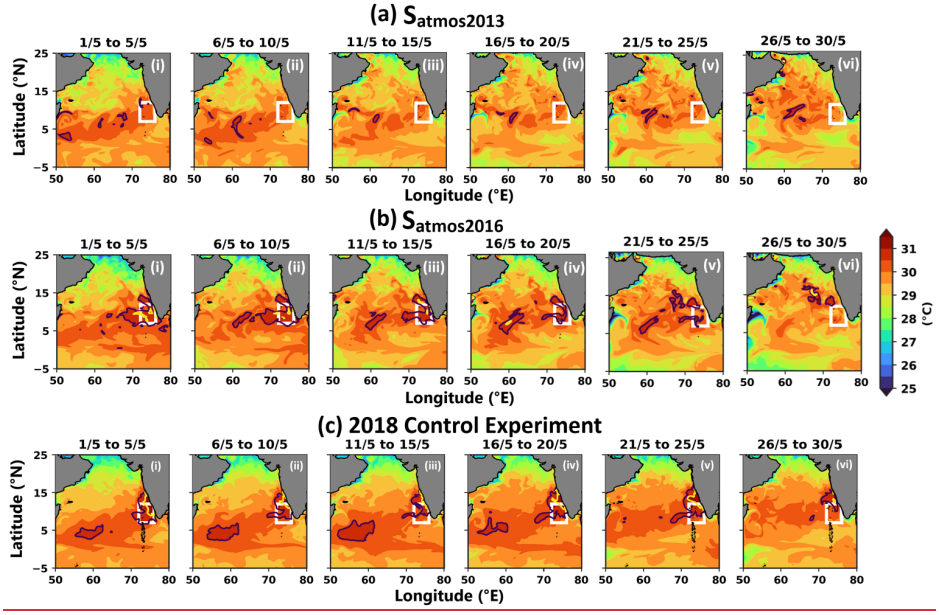

Figure 10: 5-day average evolution of SST from May 1 to May 30 for the experiment (a) $S_{ocean2013}$, (b) $S_{ocean2016}$, and (c) 2018 control experiment. In these two experiments, the atmospheric condition was replaced in 2013 and 2016 in the 2018 control experiment. See Table 1 for further details about the experiments. The black and yellow contours represent 30.5°C and 31°C, respectively. The days associated with mean evolution are displayed at the top of each subplot. The white box is the core MWP region.

The mixed layer heat budget in the core region of the MWP (72-76°E and 7-13°N) is analyzed to allow a better understanding of the factors contributing to its expansion and dissipation. The atmospheric conditions remain unchanged in the $S_{ocean2013}$, $S_{ocean2016}$, and 2018 control experiments. A dip in the net surface heat flux from 0.1°C.day^{-1} to -0.07°C.day^{-1} is noticed on May 8 in these three experiments. Later, this net surface heat flux supplied to the mixed layer temperature tendency with a maximum of 0.1°C per day from May 15 to May 18 (Fig. 11a, 11d, and 11e), and the MWP matured on May 20 thereafter. During the dissipation phase of the MWP, the net surface heat flux had an adverse impact on the temperature

Formatted: Font color: Auto

Formatted: Header, Border: Top: (No border), Bottom: (No border), Left: (No border), Right: (No border), Between : (No border), Tab stops: Not at 3.25" + 6.5"

Formatted: Font color: Auto

Formatted: Footer, Border: Top: (No border), Bottom: (No border), Left: (No border), Right: (No border), Between : (No border), Tab stops: Not at 3.25" + 6.5"

tendency in $S_{ocean2013}$, $S_{ocean2016}$, and 2018 control experiments. The vertical processes also had a cooling effect on the temperature tendency, which peaked at -0.09°C.day^{-1} on May 26 in $S_{ocean2013}$, $S_{ocean2016}$, and 2018 control experiments. Even if the MWP was not apparent in the 2013 and $S_{atmos2013}$ experiments (both of these experiments have similar atmospheric conditions), the net surface heat flux caused a gain of 0.05ºC temperature within the mixed layer on May 20 (Fig. 11b and 11f). Once the MWP reached its mature day, the vertical processes and the net surface heat flux had a detrimental effect on the temperature tendency in the $S_{atmos2016}$ and 2016 control experiments (Fig. 11c and 11g). In all control and sensitivity experiments, the temperature tendency is negatively impacted by the vertical processes during May and June; nevertheless, the net surface heat flux is the primary driver behind the variation of the temperature tendency from the mature to the dissipation day. The horizontal advection had a very minimal influence on the temperature tendency. Thus, atmospheric conditions modulate the mature and dissipation of the MWP.

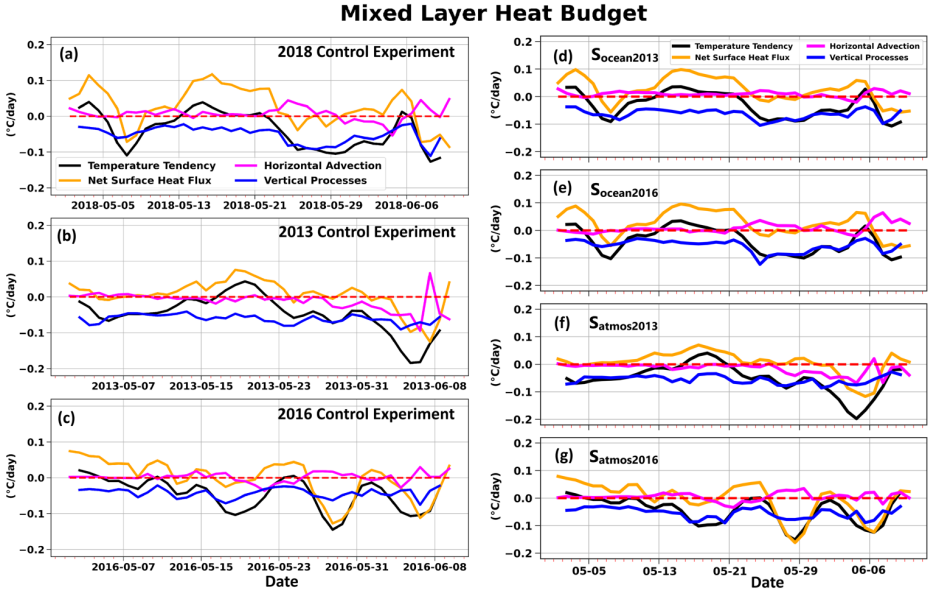

Figure 11: Area averaged (72- 76ºE and 7-13ºN, i.e., the white box shown in Fig. 1) mixed layer heat budget for three control ((a) 2018 control experiment, (b) 2013 control experiment, and (c) 2016 control experiment) and four sensitivity experiments ((d) $S_{ocean2013}$, (e) $S_{ocean2016}$, (f)$S_{atmos2013}$, and (g) $S_{atmos2016}$). In the sensitivity experiments, the oceanic and atmospheric conditions have been changed to various years; thus, only the day and month are kept on the x-axis (d to g). The mixed layer heat budget is shown for a more extended time in response to the 2nd reviewer's comment (see 1st comment in https://doi.org/10.5194/egusphere-2024-2848-RC2).

Formatted: Font color: Auto

Formatted: Header, Border: Top: (No border), Bottom: (No border), Left: (No border), Right: (No border), Between : (No border), Tab stops: Not at 3.25" + 6.5"

Formatted: Font color: Auto

Formatted: Footer, Border: Top: (No border), Bottom: (No border), Left: (No border), Right: (No border), Between : (No border), Tab stops: Not at 3.25" + 6.5"

To better assess the atmosphere's and ocean's relative contribution to the MWP intensity across different experiments, we introduced the MWP intensity index. This index is defined as:

$$MWP\ intensity\ index\ =\ MWP\ area\ on\ mature\ day\ X\ \Delta T_{avg}$$

Where ΔT_{avg} represented the average temperature change within the MWP area from its initial condition to the mature day.

In the 2016 control experiment, the MWP intensity index reached its highest value, corresponding to the warmest MWP SST and the most extensive area (Fig. 12). In contrast, the MWP was weak in the 2013 control experiment, and so as the MWP intensity index. In the $S_{ocean2013}$ experiment, where the ocean's initial and boundary conditions were modified from 2018 to 2013, the MWP Intensity Index decreased by 8.5% compared to the 2018 control experiment. However, a significant 82% reduction in the MWP intensity index was found when the atmospheric forcings were altered to 2013 in the $S_{atmos2013}$ experiment, highlighting the adverse effect of the atmospheric environment on the formation of MWP.

Conversely, the $S_{ocean2016}$ experiment, which replaced the 2018 oceanic initial and boundary condition with that of 2016, showed a 136% rise in the MWP intensity index compared to the 2018 control experiment. However, when the atmospheric condition was adjusted to 2016 in the $S_{atmos2016}$ experiment, the MWP intensity index decreased by 41%, indicating that the ocean precondition was the primary factor in the genesis of the intense MWP in 2016 and that the atmospheric condition later favored its development (Fig. 12).

Formatted: Font color: Auto

Formatted: Header, Border: Top: (No border), Bottom: (No border), Left: (No border), Right: (No border), Between : (No border), Tab stops: Not at 3.25" + 6.5"

Formatted: Left, Line spacing: single

Deleted: an index called

Deleted: represents

Formatted: Left

Deleted: opposite trend

Deleted: observed

Deleted: .

Deleted: condition was

Deleted: if the ocean's initial condition from 2016 replaced that of the 2018 control experiment ($S_{ocean2016}$).

Deleted: is

Deleted: Index

Formatted: Font color: Auto

Formatted: Footer, Border: Top: (No border), Bottom: (No border), Left: (No border), Right: (No border), Between : (No border), Tab stops: Not at 3.25" + 6.5"

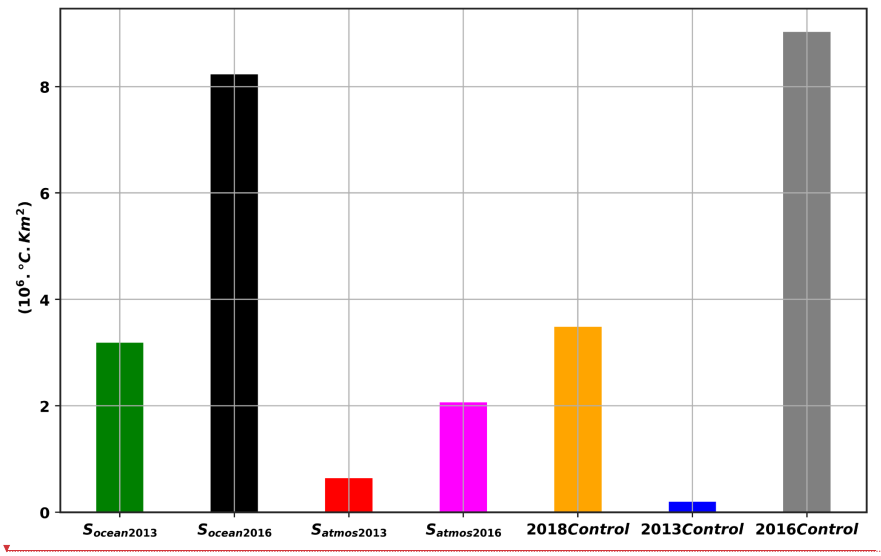

Figure 12: A comparison of the MWP intensity index in all three experiments during the respective mature phase days in different years. In $S_{ocean2013}$, $S_{ocean2016}$, $S_{atmos2013}$, 2013 control experiment, and 2018 control experiment, the mature day was May 20. In the $S_{atmos2016}$ and 2016 control experiments, the mature day was May 4.

3.3.2 Impact of Ocean Surface Flux in the Formation of the MWP

Once the ocean precondition was met, the atmospheric factors, including net surface heat flux, wind, and freshwater flux, played a leading role in shaping the spatial extent of MWP. The relative importance of net thermal flux, freshwater flux, and wind on mixing was examined here using potential turbulent kinetic energy (P_{TKE}). Contrary to wind stirring, the P_{TKE} by haline and thermal buoyancy flux was minimal in all the experiments, indicating that the wind was the driver for the mixing

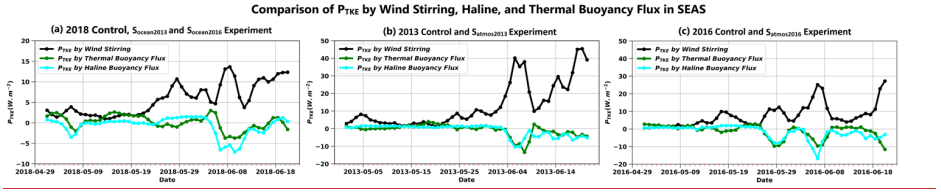

Fig. 13 Comparision of PTKE by wind, thermal, and haline buoyancy flux averaged in the SEAS (72-76°E and 7-13°N) from May 1 to June 20. The values are shown here after multiplying 10^4.

Formatted: Font color: Auto
Formatted: Header, Border: Top: (No border), Bottom: (No border), Left: (No border), Right: (No border), Between : (No border), Tab stops: Not at 3.25" + 6.5"
Deleted: ¶ ... [96]
Formatted: Left
Formatted: Font: Not Italic
Formatted: Bullets and Numbering
Deleted: is
Deleted: play
Deleted: is
Deleted: is
Deleted: is
Moved (insertion) [9]
Deleted: in
Deleted: in
Deleted: (Fig 13
Deleted: 15).
Formatted: Font:
Formatted: Font color: Auto
Formatted ... [95]

in SEAS in May (Fig. 13). The atmospheric conditions were similar in the 2018 control, $S_{ocean2013}$, and $S_{ocean2016}$ experiments (see Table 1 for experiment details). From 1st to 5th May, the average P_{TKE} caused by wind stirring was more than 8 $W.m^{-2}$; however, in the SEAS, a small wind shadow zone was formed with a very low P_{TKE} (Fig. 14a). Subsequently, the mixing reduced, and expansion of MWP SST was observed within this wind shadow zone in 2018 control, $S_{ocean2013}$, and $S_{ocean2016}$ experiments. A similar but much-widened wind shadow zone was developed in the SEAS from 17th to 20th May, resulting in the largest MWP expansion in 2018 control, $S_{ocean2013}$, and $S_{ocean2016}$ experiments. Once the southwesterly wind strengthened, the P_{TKE} increased, and the ocean lost heat at the surface (Fig. 13a and 14a). In the 2013 control and $S_{atmos2013}$ experiments, atmospheric conditions were identical, and the ocean gained heat (Fig. S11b in the supplementary). The wind-induced P_{TKE} was more in SEAS, and no such wind shadow zone was developed (Fig 14b). Subsequently, the MWP was absent in these two experiments. In the 2016 control and $S_{atmos2016}$ experiments, the wind shadow zone was unfurled over a comparatively large area from the 1st to the 8th of May (Fig. 14c). Besides, the ocean received heat during this time in SEAS, making a favorable condition for the development of the strong MWP (Fig. 11c in supplementary).

Formatted: Font color: Auto

Formatted: Header, Border: Top: (No border), Bottom: (No border), Left: (No border), Right: (No border), Between : (No border), Tab stops: Not at 3.25" + 6.5"

Deleted: are

Deleted: .

Formatted: Left, Indent: First line: 0", Line spacing: single

Deleted: is

Deleted: is

Deleted: 13

Deleted: reduces

Deleted: is

Deleted: southeastern Arabian Sea

Deleted: strengthens

Deleted: increases

Deleted: loses

Deleted: 13

Deleted: SEAS. Nonetheless, the

Deleted: 14

Deleted: , indicating that the net heat flux alone can't forge an MWP-like condition

Deleted: 15

Deleted: receives

Deleted: MWP once the ocean precondition is favorable

Deleted: 15

Formatted: Font color: Auto

Formatted: Footer, Border: Top: (No border), Bottom: (No border), Left: (No border), Right: (No border), Between : (No border), Tab stops: Not at 3.25" + 6.5"

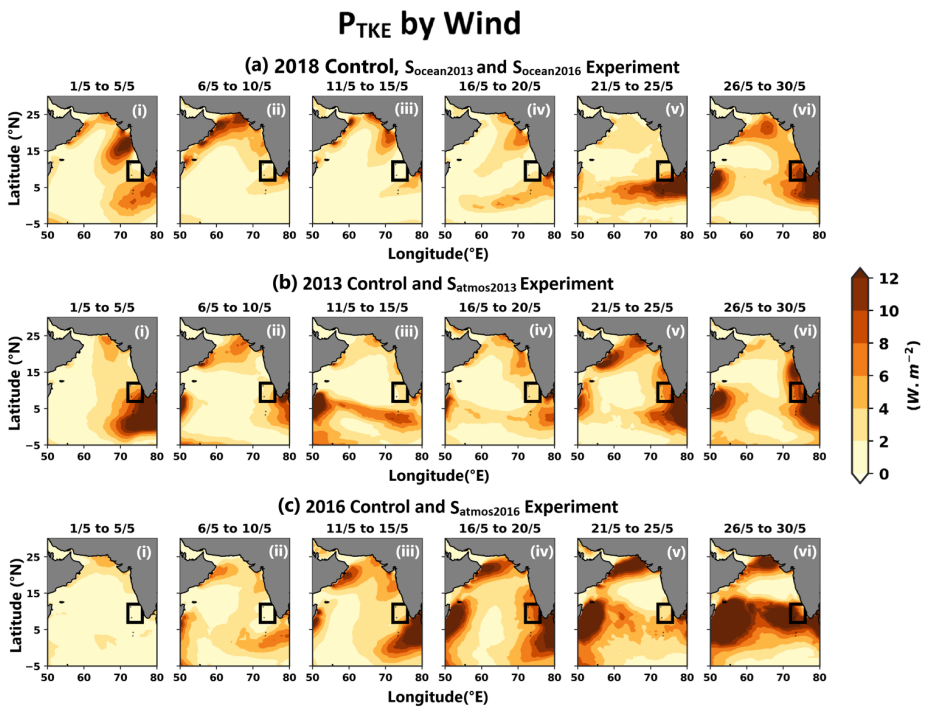

Figure 14: 5-day average evolution of wind-induced production of turbulent kinetic energy (P_{TKE}) for all control and sensitivity experiments. The fill values are showing after multiplying 10^4. Atmospheric forcings are identical for the 2018 control, $S_{ocean2013}$, and $S_{ocean2016}$ experiments. Likewise, the P_{TKE} remains the same across all three experiments (a). Similarly, the P_{TKE} owing to thermal buoyancy flux in the 2013 control experiment and $S_{ocean2013}$ (b) and the 2016 control experiment and $S_{ocean2016}$ (c) are identical. Table 1 shows details from the sensitivity experiments. The days associated with mean evolution are listed at the top of each subplot.

Formatted: Font color: Auto

Formatted: Header, Border: Top: (No border), Bottom: (No border), Left: (No border), Right: (No border), Between : (No border), Tab stops: Not at 3.25" + 6.5"

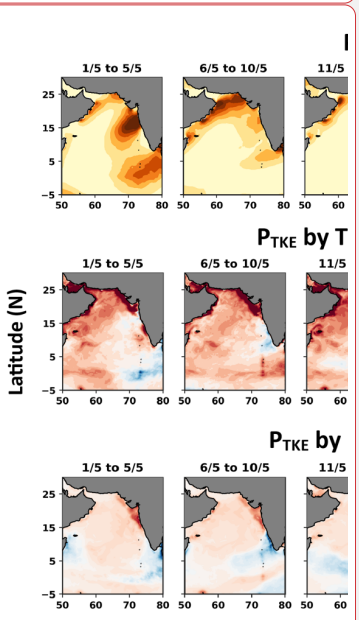

Deleted:

Moved up [9]: Fig.

Deleted: 13…5-day average evolution of different components of the…ind-induced production of total…urbulent kinetic energy in the 2018…(P_{TKE}) for all control experiment. In … [97]

Formatted: Left

Deleted: …xperiments,… Likewise, the P_{TKE} remains the atmospheric condition is similar to …ame across all three experiments (a). Similarly, the 2018 control simulation. … [98]

Formatted: Font: Not Superscript/ Subscript

Formatted … [99]

Deleted: . Details of…(c) are identical. Table 1 shows details from the sensitivity experiments are depicted in Table … [100]

Formatted: Font: Bold

Deleted: displayed

Formatted: Caption, Left, Indent: First line: 0", Line spacing: single

Formatted: Left, Line spacing: single

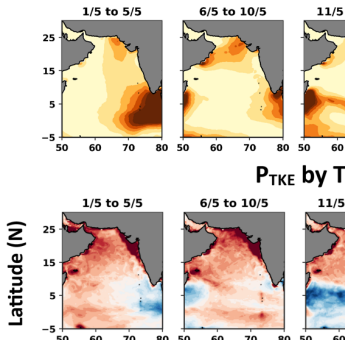

4 Conclusion

A coupled atmosphere-ocean numerical model has been employed to investigate the formation and evolution of the MWP in the SEAS. The model is simulated for three independent years: 2013, 2016, and 2018. The simulated results can reproduce the MWP features and showed good agreement with satellite and buoy data (Fig. 2 to 5 and Fig. S2 to S5 in supplementary). The evolution of the atmospheric and ocean features near the SEAS from mature to dissipation day is well represented in the model. Four sensitivity experiments further elucidated the roles of oceanic and atmospheric conditions in the MWP formation. The changes in ocean initial conditions substantially impacted the magnitude of the MWP core temperature, resulting in 0.6ºC higher in $S_{ocean2016}$ and 0.3ºC lower in $S_{ocean2013}$ compared to the 2018 control experiment (Fig. S10d and S10e are compared with Fig. S10a in the supplementary), indicating the influence of the ocean initial condition in the MWP intensity. Analysis of the mixed-layer heat budget (Fig. 11) revealed that net surface heat flux is the primary driver of the MWP development, contributing significantly to the increase in mixed-layer temperature in the control and sensitivity experiments. It contributed more than 0.1°C per day to the increased temperature just before the MWP matured on the day of 2018. Vertical processes negatively affected temperature tendencies and could reach as high as -0.08ºC/day. As the moisture-rich southwesterly wind strengthened in late May to early June, it caused cloudiness, blocking the incoming shortwave radiation and the loss of latent heat flux in the SEAS (Fig S6 and S8 in supplementary). Thus, the net surface heat flux emerges as the primary driver behind the dissipation of the MWP (Fig. 11).

The change in atmospheric conditions in $S_{atmos2013}$ and $S_{atmos2016}$ has altered the roles of net surface heat flux and vertical processes in temperature tendencies of the heat budget. Besides, the atmospheric conditions remain the same in the 2018 control experiment, $S_{ocean2013}$, and $S_{ocean2016}$. Likewise, the contribution of net surface heat flux and the vertical processes on the mixed layer temperature tendency has shown identical variability. This net surface heat flux, along with the vertical process, was responsible for the dissipation of the MWP, indicating that the atmospheric processes control the MWP's advancement from mature to dissipation day. Subsequently, the MWP intensity index revealed that shuffling of the atmospheric forcings and oceanic initial conditions of the strong MWP year to the year of the MWP whose intensity was identical to climatology ($S_{atmos2016}$ and $S_{ocean2016}$ experiment) resulted in a substantial rise of 41% and 136% in MWP intensity index respectively (Fig. 12), which demonstrated that in the strong MWP year, the pre-April ocean condition played a considerable role in the development of the MWP in May which was further supported by the prevailing atmospheric conditions. The exchange of atmospheric forcings from the weak MWP years to the year of the MWP whose intensity is similar to climatology ($S_{atmos2013}$ and $S_{atmos2016}$ experiment) resulted in a decrease of 82% and 8.5% in the MWP's intensity, respectively, suggesting that in the weak MWP year, although the ocean preconditions were met, it's the atmospheric forcing that restricted the development of the MWP in SEAS.

Later, P_{TKE} was computed to study the mixing in the SEAS. The influence of wind-induced P_{TKE} on mixing surpassed that of P_{TKE} caused due to thermal and haline buoyancy flux (Fig. 13). Further, a wind shadow zone with less P_{TKE} was witnessed in SEAS. The MWP advanced within this zone (Fig. 14). However, this shadow zone was not present in experiments such as the

Formatted: Font color: Auto

Formatted: Header, Border: Top: (No border), Bottom: (No border), Left: (No border), Right: (No border), Between : (No border), Tab stops: Not at 3.25" + 6.5"

Deleted: was…as been employed to investigate the formation and evolution of the MWP in the southeastern Arabian Sea. …EAS. The model was…s simulated for three independent years: 2013, 2016, and 2018. The simulated results were able to…an reproduce the MWP features and showed good agreement with observational…atellite and buoy data. ... [102]

Moved down [10]: Analysis of the mixed-layer heat budget (Fig.

Deleted: 8) revealed that net heat flux is the primary driver of the MWP development, contributing significantly to the increase in mixed-layer temperature. It contributed more than 0.1°C per day to the increased temperature throughout the MWP development phase. However, net heat flux alone does not fully account for the regional expansion of warm SST observed in the SEAS. Once the MWP reaches its …ature phase, vertical processes negatively affect temperature tendencies by -0.08ºC/day, leading to its rapid …o dissipation. Additionally, four…day is well represented in the model. Four sensitivity experiments further elucidated the roles of oceanic and atmospheric conditions in the MWP formation. The changes in ocean initial conditions significantly…ubstantially impacted the magnitude of the MWP core temperature, resulting in 0.6ºC higher in $S_{ocean2016}$ and 0.3ºC lower in $S_{ocean2013}$ compared to the 2018 control experiment (Fig. S7a…10d and S7c…10e are compared with Fig. 8a ... [103]

Moved (insertion) [10]

Formatted: Left, Line spacing: single

Deleted: This vertical process is …esides, the atmospheric conditions remain the same in the 2018 control experiment, $S_{ocean2013}$, and $S_{ocean2016}$. Likewise, the contribution of net surface heat flux and the vertical processes on the mixed layer temperature tendency has shown identical variability. This net surface heat flux, along with the vertical process, was responsible for the dissipation of the MWP.… indicating that the atmospheric processes control the MWP's advancement from mature to dissipation day. Subsequently, the MWP intensity index reveals…evealed that shuffling of the atmospheric forcings and oceanic initial conditions of the strong MWP year to the year of the MWP whose intensity is…as identical to climatology (see the details of the experiment …$_{atmos2016}$ and $S_{ocean2016}$) results…experiment) resulted in a substantial rise of 41% 136% in MWP intensity index respectively,…(Fig. 12), which demonstrates…emonstrated that in the strong MWP year, the pre-April ocean condition plays…layed a considerable role in the development of the MWP in May which is…as further supported by the prevailing atmospheric conditions. This contradicts pre ... [104]

Deleted: …induced P_{TKE} on mixing far surpasses…urpassed that of P_{TKE} resulting from …aused due to thermal and haline buoyancy flux.…(Fig. 13). Further, a wind shadow zone with less P_{T} ... [105]

Formatted: Left, Indent: First line: 0", Line spacing: single

Formatted: Font color: Auto

Formatted: Footer, Border: Top: (No border), Bottom: (No border), Left: (No border), Right: (No border), Between : (No border), Tab stops: Not at 3.25" + 6.5"

2013 control and $S_{atmos2013}$ experiment. The MWP did not develop in these two experiments, although the ocean preconditions were met, indicating that the wind shadow zone was a key factor in the MWP's advancement within the SEAS.

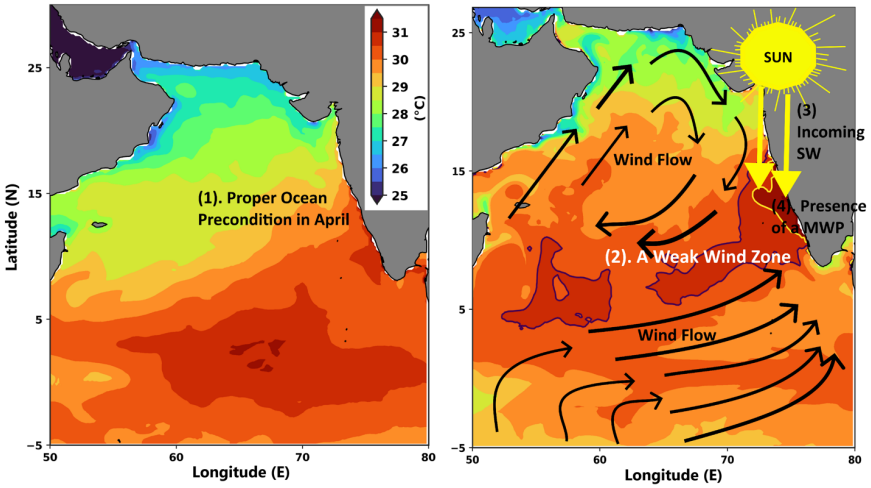

Figure 15 Schematic of the atmospheric and oceanic conditions associated with the formation of the MWP. The numbering denotes the importance of that process in the formation of MWP. For instance, the ocean precondition (1) is the first requirement for MWP's genesis. Later, a weak wind zone (2) with less mixing traps the incoming shortwave radiation (3) in SEAS, which results in the formation of the MWP (4). Both the subplots have the same color bar levels. The black and yellow contours represent 30.5ºC and 31ºC, respectively.

In conclusion, once the ocean conditions before April have laid the foundation ((1) in Fig. 15), the prevailing atmospheric conditions develop a weak wind zone in SEAS in May ((2) in Fig. 15), and the incoming shortwave radiation flux under the clear sky is trapped within this zone ((3) in Fig. 15). Subsequently, the MWP advances inside this area. Thus, a strong MWP can only occur in SEAS if all of these requirements are met (Fig. 15). After the MWP matures, the strong southwesterly wind in SEAS causes cloudiness and enhances P_{TKE}, which blocks the incoming shortwave radiation and leads to MWP's dissipation due to decrease in the net surface heat flux. Therefore, the MWP's genesis to dissipation mechanism is a completely coupled process influenced by both ocean preconditions and atmospheric forcings, and the coupled atmosphere-ocean numerical model has proved to be an excellent tool in understanding this complex interaction. Furthermore, 2016 was a strong El Niño year, and the impact of winter salinity stratification in such intense El Niño years on the pre-April SST is a subject for future scope of research. Given that the wind shadow zone emerges during a year with high MWP SST, we hypothesize that this zone and the corresponding increase in MWP SST could be associated with the onset of the Indian Summer Monsoon. However, additional investigation is necessary, which is beyond the scope of the present study.

Formatted: Font color: Auto

Formatted: Header, Border: Top: (No border), Bottom: (No border), Left: (No border), Right: (No border), Between : (No border), Tab stops: Not at 3.25" + 6.5"

Deleted: , this shadow zone was not present, and the

Formatted: Left, Line spacing: single

Deleted: Fig. 16

Formatted: Left

Deleted: ¶

Deleted: formation

Deleted: of the MWP

Deleted: fully

Deleted: driven

Deleted: (Fig. 16). The

Deleted: essential

Deleted: for

Deleted: However, further modeling efforts are required to better understand the air-sea interaction during the MWP mature phase.

Deleted: -Nino

Deleted: -Nino

Deleted: Moreover, given

Deleted: current

Formatted: Font color: Auto

Formatted: Footer, Border: Top: (No border), Bottom: (No border), Left: (No border), Right: (No border), Between : (No border), Tab stops: Not at 3.25" + 6.5"

Data Availability:

SODA3.4.2 data is used to give initial and boundary conditions to the ocean part of the numerical model (Carton et al., 2018), whereas ERA5 data is used for the atmospheric boundary and initial condition (Hersbach et al., 2020). NOAA-AVHRR SST data is downloaded from https://www.ncei.noaa.gov/products/avhrr-pathfinder-sst (Saha et al., 2018). OSCAR current data is used to validate the model (Bonjean & Lagerloef, 2002). AD10 moored buoy data is available in the INCOIS data portal (https://incois.gov.in/portal/datainfo/mb.jsp). All the model output data used in this study are available upon request.

Software Availability:

Authors gratefully acknowledge USGS for making the COAWST numerical model available openly. In this study, python is used for the graphical plots. In addition, the Gibbs Seawater package (McDougall & Barker 2011) (https://www.teos-10.org/software.htm#1) is utilized to compute basic oceanic parameters. Further, wrf-python is utilized to handle the WRF output (Ladwig 2017). Software/programs related to the study may be available from the corresponding author upon request.

Author Contributions:

SPL ran the numerical models, analyzed the results, and wrote the first draft of the manuscript. KRP helped in analysis and manuscript editing. VP reviewed the manuscript and supervised the work. All the authors agreed to the final version of the manuscript.

Competing Interests:

The contact author has declared that none of the authors has any competing interests.

Acknowledgments

This work is a part of SPL's doctoral thesis work. SPL is grateful to the Ministry of Education, Government of India, for awarding the Prime Minister's Research Fellowship (Ref: IITD/Admission/Ph.D./PMRF/2020-21/380299) for pursuing his doctoral research work at IIT-Delhi, India. The computational resources acquired through the high-performance computing (HPC) cluster at the IIT-Delhi are acknowledged. We thank the two anonymous reviewers for their insightful comments.

References

Abram, N. J., Gagan, M. K., McCulloch, M. T., Chappell, J., & Hantoro, W. S. (2003). Coral reef death during the 1997 Indian Ocean Dipole linked to Indonesian wildfires. *Science*, *301*(5635). https://doi.org/10.1126/science.1083841

Formatted: Font color: Auto
Formatted: Header, Border: Top: (No border), Bottom: (No border), Left: (No border), Right: (No border), Between : (No border), Tab stops: Not at 3.25" + 6.5"
Deleted: ¶
Formatted: Left, Indent: First line: 0", Line spacing: single
Deleted: condition
Formatted: Font color: Auto
Deleted: may be
Deleted: on
Deleted: to the author.
Formatted: Left, Line spacing: single
Formatted: Left, Line spacing: single
Formatted: Font:
Deleted: sincerely acknowledge
Deleted: financial support
Formatted: Left, Line spacing: single
Deleted: Minister's
Deleted:).
Deleted: Indian Institute of Technology
Deleted: ¶
Formatted: Font color: Auto
Formatted: Font: 12 pt, Font color: Auto
Formatted: Font color: Auto
Formatted: Footer, Border: Top: (No border), Bottom: (No border), Left: (No border), Right: (No border), Between : (No border), Tab stops: Not at 3.25" + 6.5"

Akhil, V. P., Lengaigne, M., Krishnamohan, K. S., Keerthi, M. G., & Vialard, J. (2023). Southeastern Arabian Sea Salinity variability: mechanisms and influence on surface temperature. *Climate Dynamics*, *61*(7–8). https://doi.org/10.1007/s00382-023-06765-z

ARAKAWA, A., & LAMB, V. R. (1977). *Computational Design of the Basic Dynamical Processes of the UCLA General Circulation Model*. https://doi.org/10.1016/b978-0-12-460817-7.50009-4

Banzon, V., Smith, T. M., Mike Chin, T., Liu, C., & Hankins, W. (2016). A long-term record of blended satellite and in situ sea-surface temperature for climate monitoring, modeling and environmental studies. *Earth System Science Data*, *8*(1). https://doi.org/10.5194/essd-8-165-2016

Bonjean, F., & Lagerloef, G. S. E. (2002). Diagnostic model and analysis of the surface currents in the Tropical Pacific Ocean. *Journal of Physical Oceanography*, *32*(10). https://doi.org/10.1175/1520-0485(2002)032<2938:DMAAOT>2.0.CO;2

Boutin, J., Reul, N., Koehler, J., Martin, A., Catany, R., Guimbard, S., Rouffi, F., Vergely, J. L., Arias, M., Chakroun, M., Corato, G., Estella-Perez, V., Hasson, A., Josey, S., Khvorostyanov, D., Kolodziejczyk, N., Mignot, J., Olivier, L., Reverdin, G., … Mecklenburg, S. (2021). Satellite-Based Sea Surface Salinity Designed for Ocean and Climate Studies. *Journal of Geophysical Research: Oceans*, *126*(11). https://doi.org/10.1029/2021JC017676

Bruce, J. G., Johnson, D. R., & Kindle, J. C. (1994). Evidence for eddy formation in the eastern Arabian Sea during the northeast monsoon. *Journal of Geophysical Research*, *99*(C4). https://doi.org/10.1029/94JC00035

Bruce, J. G., Kindle, J. C., Kantha, L. H., Kerling, J. L., & Bailey, J. F. (1998). Recent observations and modeling in the Arabian Sea laccadive high region. *Journal of Geophysical Research: Oceans*, *103*(3334). https://doi.org/10.1029/97jc03219

Carniel, S., Benetazzo, A., Bonaldo, D., Falcieri, F. M., Miglietta, M. M., Ricchi, A., & Sclavo, M. (2016). Scratching beneath the surface while coupling atmosphere, ocean and waves: Analysis of a dense water formation event. *Ocean Modelling*, *101*. https://doi.org/10.1016/j.ocemod.2016.03.007

Carton, J. A., Chepurin, G. A., & Chen, L. (2018). SODA3: A new ocean climate reanalysis. *Journal of Climate*, *31*(17). https://doi.org/10.1175/jcli-d-18-0149.1

Chakraborty, T., Pattnaik, S., & Baisya, H. (2023). Investigating the precipitation features of monsoon deep depressions over the Bay of Bengal using high-resolution stand-alone and coupled simulations. *Quarterly Journal of the Royal Meteorological Society*, *149*(753). https://doi.org/10.1002/qj.4449

Chakraborty, T., Pattnaik, S., Baisya, H., & Vishwakarma, V. (2022). Investigation of Ocean Sub-Surface Processes in Tropical Cyclone Phailin Using a Coupled Modeling Framework: Sensitivity to Ocean Conditions. *Oceans*, *3*(3). https://doi.org/10.3390/oceans3030025

Dai, Q., Han, D., Rico-Ramirez, M. A., & Islam, T. (2013). The impact of raindrop drift in a three-dimensional wind field on a radar-gauge rainfall comparison. *International Journal of Remote Sensing*, *34*(21). https://doi.org/10.1080/01431161.2013.826838

Formatted: Font color: Auto

Formatted: Header, Border: Top: (No border), Bottom: (No border), Left: (No border), Right: (No border), Between : (No border), Tab stops: Not at 3.25" + 6.5"

Formatted: Font color: Auto

Deleted: Arakawa

Deleted: Lamb

Formatted: Font color: Auto

Formatted: Font color: Auto

Formatted: Font color: Auto

Formatted: Left

Formatted: Font color: Auto

Formatted: Left

Formatted: Font color: Auto

Formatted: Footer, Border: Top: (No border), Bottom: (No border), Left: (No border), Right: (No border), Between : (No border), Tab stops: Not at 3.25" + 6.5"

Deepa, R., Seetaramayya, P., Nagar, S. G., & Gnanaseelan, C. (2007). On the plausible reasons for the formation of onset vortex in the presence of Arabian Sea mini warm pool. *Current Science*, *92*(6).

Doval, M. D., & Hansell, D. A. (2000). Organic carbon and apparent oxygen utilization in the western South Pacific and the central Indian Oceans. *Marine Chemistry*, *68*(3). https://doi.org/10.1016/S0304-4203(99)00081-X

Dudhia, J. (1989). Numerical study of convection observed during the Winter Monsoon Experiment using a mesoscale two-dimensional model. *Journal of the Atmospheric Sciences*, *46*(20). https://doi.org/10.1175/1520-0469(1989)046<3077:NSOCOD>2.0.CO;2

Durand, F., Shankar, D., de Boyer Montégut, C., Shenoi, S. S. C., Blanke, B., & Madec, G. (2007). Modeling the barrier-layer formation in the southeastern Arabian Sea. *Journal of Climate*, *20*(10). https://doi.org/10.1175/JCLI4112.1

Durand, F., Shetye, S. R., Vialard, J., Shankar, D., Shenoi, S. S. C., Ethe, C., & Madec, G. (2004). Impact of temperature inversions on SST evolution in the South-Eastern Arabian Sea during the pre-summer monsoon season. *Geophysical Research Letters*, *31*(1). https://doi.org/10.1029/2003GL018906

Foltz, G. R., & McPhaden, M. J. (2009). Impact of barrier layer thickness on SST in the central tropical North Atlantic. *Journal of Climate*, *22*(2). https://doi.org/10.1175/2008JCLI2308.1

Girishkumar, M. S., Joseph, J., Thangaprakash, V. P., Pottapinjara, V., & McPhaden, M. J. (2017). Mixed Layer Temperature Budget for the Northward Propagating Summer Monsoon Intraseasonal Oscillation (MISO) in the Central Bay of Bengal. *Journal of Geophysical Research: Oceans*, *122*(11). https://doi.org/10.1002/2017JC013073

Gopalakrishna, V. V., Johnson, Z., Salgaonkar, G., Nisha, K., Rajan, C. K., & Rao, R. R. (2005). Observed variability of sea surface salinity and thermal inversions in the Lakshadweep Sea during contrast monsoons. *Geophysical Research Letters*, *32*(18). https://doi.org/10.1029/2005GL023280

Haidvogel, D. B., Arango, H. G., Hedstrom, K., Beckmann, A., Malanotte-Rizzoli, P., & Shchepetkin, A. F. (2000). Model evaluation experiments in the North Atlantic Basin: Simulations in nonlinear terrain-following coordinates. *Dynamics of Atmospheres and Oceans*, *32*(3–4). https://doi.org/10.1016/S0377-0265(00)00049-X

Han, W., McCreary, J. P., & Kohler, K. E. (2001). Influence of precipitation minus evaporation and Bay of Bengal rivers on dynamics, thermodynamics, and mixed layer physics in the upper Indian Ocean. *Journal of Geophysical Research: Oceans*, *106*(C4). https://doi.org/10.1029/2000jc000403

Hareesh Kumar, P. V., Joshi, M., Sanilkumar, K. V., Rao, A. D., Anand, P., Anil Kumar, K., & Prasada Rao, C. V. K. (2009). Growth and decay of the Arabian Sea mini warm pool during May 2000: Observations and simulations. *Deep-Sea Research Part I: Oceanographic Research Papers*, *56*(4). https://doi.org/10.1016/j.dsr.2008.12.004

Hareesh Kumar, P. V., Sanilkumar, K. V., & Prasada Rao, C. V. K. (2007). Arabian sea mini warm pool and its influence on acoustic propagation. *Defence Science Journal*, *57*(1). https://doi.org/10.14429/dsj.57.1738

Hastenrath, S., & Greischar, L. L. (1989). Climatic atlas of the Indian Ocean. Part III: upper-ocean structure. *Climatic Atlas of the Indian Ocean. Part III: Upper-Ocean Structure*. https://doi.org/10.2307/635289

Formatted: Font color: Auto

Formatted: Header, Border: Top: (No border), Bottom: (No border), Left: (No border), Right: (No border), Between : (No border), Tab stops: Not at 3.25" + 6.5"

Formatted: Font color: Auto

Formatted: Footer, Border: Top: (No border), Bottom: (No border), Left: (No border), Right: (No border), Between : (No border), Tab stops: Not at 3.25" + 6.5"

He, Q., Zhan, H., & Cai, S. (2020). Anticyclonic Eddies Enhance the Winter Barrier Layer and Surface Cooling in the Bay of Bengal. *Journal of Geophysical Research: Oceans*, *125*(10). https://doi.org/10.1029/2020JC016524

Hersbach, H., Bell, B., Berrisford, P., Hirahara, S., Horányi, A., Muñoz-Sabater, J., Nicolas, J., Peubey, C., Radu, R., Schepers, D., Simmons, A., Soci, C., Abdalla, S., Abellan, X., Balsamo, G., Bechtold, P., Biavati, G., Bidlot, J., Bonavita, M., … Thépaut, J. N. (2020). The ERA5 global reanalysis. *Quarterly Journal of the Royal Meteorological Society*, *146*(730). https://doi.org/10.1002/qj.3803

Hong, S. Y., Noh, Y., & Dudhia, J. (2006). A new vertical diffusion package with an explicit treatment of entrainment processes. *Monthly Weather Review*, *134*(9). https://doi.org/10.1175/MWR3199.1

Jacob, R., Larson, J., & Ong, E. (2005). M × N communication and parallel interpolation in community climate system model version 3 using the model coupling toolkit. *International Journal of High Performance Computing Applications*, *19*(3). https://doi.org/10.1177/1094342005056116

Kara, A. B., Rochford, P. A., & Hurlburt, H. E. (2000). An optimal definition for ocean mixed layer depth. *Journal of Geophysical Research: Oceans*, *105*(C7). https://doi.org/10.1029/2000jc900072

Kurian, J., & Vinayachandran, P. N. (2007). Mechanisms of formation of the Arabian Sea mini warm pool in a high-resolution Ocean General Circulation Model. *Journal of Geophysical Research: Oceans*, *112*(5). https://doi.org/10.1029/2006JC003631

Ladwig, W. (2017). *wrf-python (Version 1.3.2)*.

Large, W. G., McWilliams, J. C., & Doney, S. C. (1994). Oceanic vertical mixing: A review and a model with a nonlocal boundary layer parameterization. In *Reviews of Geophysics* (Vol. 32, Issue 4). https://doi.org/10.1029/94RG01872

Large, W. G., & Pond, S. (1981). Open ocean momentum flux measurements in moderate to strong winds. *J. PHYS. OCEANOGR.*, *11*(3, Mar. 1981). https://doi.org/10.1175/1520-0485(1981)011<0324:oomfmi>2.0.co;2

Li, N., Zhu, X., Wang, H., Zhang, S., & Wang, X. (2023). Intraseasonal and interannual variability of sea temperature in the Arabian Sea Warm Pool. *Ocean Science*, *19*(5), 1437–1451. https://doi.org/10.5194/os-19-1437-2023

Lim, K. S. S., & Hong, S. Y. (2010). Development of an effective double-moment cloud microphysics scheme with prognostic cloud condensation nuclei (CCN) for weather and climate models. *Monthly Weather Review*, *138*(5). https://doi.org/10.1175/2009MWR2968.1

Lukas, R., & Lindstrom, E. (1991). The mixed layer of the western equatorial Pacific Ocean. *Journal of Geophysical Research: Oceans*, *96*(S01). https://doi.org/10.1029/90jc01951

Masson, S., Luo, J. J., Madec, G., Vialard, J., Durand, F., Gualdi, S., Guilyardi, E., Behera, S., Delecluse, P., Navarra, A., & Yamagata, T. (2005). Impact of barrier layer on winter-spring variability of the southeastern Arabian Sea. *Geophysical Research Letters*, *32*(7). https://doi.org/10.1029/2004GL021980

Mathew, S., Natesan, U., Latha, G., & Venkatesan, R. (2018). Dynamics behind warming of the southeastern Arabian Sea and its interruption based on in situ measurements. *Ocean Dynamics*, *68*(4–5). https://doi.org/10.1007/s10236-018-1130-3

Formatted: Font color: Auto

Formatted: Header, Border: Top: (No border), Bottom: (No border), Left: (No border), Right: (No border), Between : (No border), Tab stops: Not at 3.25" + 6.5"

Deleted: Kumar, S. P., & Prasad, T. G. (1999). Formation and spreading of Arabian Sea high-salinity water mass. *Journal of Geophysical Research: Oceans*, *104*(C1). https://doi.org/10.1029/1998jc900022¶

Formatted: Font color: Auto

Formatted: Font color: Auto

Formatted: Footer, Border: Top: (No border), Bottom: (No border), Left: (No border), Right: (No border), Between : (No border), Tab stops: Not at 3.25" + 6.5"

McDougall, Trevor J.; Barker, P. M. (2011). Getting started with TEOS-10 and the Gibbs Seawater (GSW) Oceanographic Toolbox. *Scor/Iapso Wg127*.

Mlawer, E. J., Taubman, S. J., Brown, P. D., Iacono, M. J., & Clough, S. A. (1997). Radiative transfer for inhomogeneous atmospheres: RRTM, a validated correlated-k model for the longwave. *Journal of Geophysical Research Atmospheres*, *102*(14). https://doi.org/10.1029/97jd00237

Murty, V. S. N., Krishna, S. M., Nagaraju, A., Somayajulu, Y. K., Babu, V. R., Sengupta, D., Sindu, P. R., Ravichandran, M., & Rajesh, G. (2006). On the warm pool dynamics in the southeastern Arabian Sea during April-May 2005 based on the satellite remote sensing and ARGO float data. *Remote Sensing of the Marine Environment*, *6406*. https://doi.org/10.1117/12.694254

Neema, C. P., Hareeshkumar, P. V., & Babu, C. A. (2012). Characteristics of Arabian Sea mini warm pool and Indian summer monsoon. *Climate Dynamics*, *38*(9–10). https://doi.org/10.1007/s00382-011-1166-2

Nigam, T., Pant, V., & Prakash, K. R. (2018). Impact of Indian ocean dipole on the coastal upwelling features off the southwest coast of India. *Ocean Dynamics*, *68*(6). https://doi.org/10.1007/s10236-018-1152-x

Nyadjro, E. S., Subrahmanyam, B., Murty, V. S. N., & Shriver, J. F. (2012). The role of salinity on the dynamics of the Arabian Sea mini warm pool. *Journal of Geophysical Research: Oceans*, *117*(9). https://doi.org/10.1029/2012JC007978

Olabarrieta, M., Warner, J. C., Armstrong, B., Zambon, J. B., & He, R. (2012). Ocean-atmosphere dynamics during Hurricane Ida and Nor'Ida: An application of the coupled ocean-atmosphere-wave-sediment transport (COAWST) modeling system. *Ocean Modelling*, *43–44*. https://doi.org/10.1016/j.ocemod.2011.12.008

Olabarrieta, M., Warner, J. C., & Kumar, N. (2011). Wave-current interaction in Willapa Bay. *Journal of Geophysical Research: Oceans*, *116*(12). https://doi.org/10.1029/2011JC007387

Paul, N., Sukhatme, J., Gayen, B., & Sengupta, D. (2023). Eddy-Freshwater Interaction Using Regional Ocean Modeling System in the Bay of Bengal. *Journal of Geophysical Research: Oceans*, *128*(4). https://doi.org/10.1029/2022JC019439

PAULSON CA. (1970). MATHEMATICAL REPRESENTATION OF WIND SPEED ND TEMPERATURE PROFILES IN THE UNSTABLE ATMOSPHERIC SURFACE LAYER. *Journal of Applied Meteorology*, *9*(6).

Phillips, N. A. (1957). A COORDINATE SYSTEM HAVING SOME SPECIAL ADVANTAGES FOR NUMERICAL FORECASTING. *Journal of Meteorology*, *14*(2). https://doi.org/10.1175/1520-0469(1957)014<0184:acshss>2.0.co;2

Prakash, K. R., Nigam, T., & Pant, V. (2018). Estimation of oceanic subsurface mixing under a severe cyclonic storm using a coupled atmosphere-ocean-wave model. *Ocean Science*, *14*(2). https://doi.org/10.5194/os-14-259-2018

Prakash, K. R., & Pant, V. (2017). Upper oceanic response to tropical cyclone Phailin in the Bay of Bengal using a coupled atmosphere-ocean model. *Ocean Dynamics*, *67*(1). https://doi.org/10.1007/s10236-016-1020-5

Formatted: Font color: Auto

Formatted: Header, Border: Top: (No border), Bottom: (No border), Left: (No border), Right: (No border), Between : (No border), Tab stops: Not at 3.25" + 6.5"

Formatted: Font color: Auto

Formatted: Footer, Border: Top: (No border), Bottom: (No border), Left: (No border), Right: (No border), Between : (No border), Tab stops: Not at 3.25" + 6.5"

Prakash, K. R., & Pant, V. (2020). On the wave-current interaction during the passage of a tropical cyclone in the Bay of Bengal. *Deep-Sea Research Part II: Topical Studies in Oceanography*, *172*. https://doi.org/10.1016/j.dsr2.2019.104658

PV Joseph. (1990). *Warm pool over the Indian Ocean and monsoon onset*.

Rao, R. R., & Sivakumar, R. (1999). On the possible mechanisms of the evolution of a mini-warm pool during the pre-summer monsoon season and the genesis of onset vortex in the South-Eastern Arabian Sea. *Quarterly Journal of the Royal Meteorological Society*, *125*(555). https://doi.org/10.1002/qj.49712555503

Rao, S. A., Gopalakrishna, V. V., Shetye, S. R., & Yamagata, T. (2002). Why were cool SST anomalies absent in the Bay of Bengal during the 1997 Indian Ocean Dipole event? *Geophysical Research Letters*, *29*(11). https://doi.org/10.1029/2001GL014645

Ricchi, A., Miglietta, M. M., Falco, P. P., Benetazzo, A., Bonaldo, D., Bergamasco, A., Sclavo, M., & Carniel, S. (2016). On the use of a coupled ocean-atmosphere-wave model during an extreme cold air outbreak over the Adriatic Sea. *Atmospheric Research*, *172–173*. https://doi.org/10.1016/j.atmosres.2015.12.023

Saha, K., Zhao, X., Zhang, H., Casey, K. S., Zhang, D., Baker-Yeboah, Sheekela., Kilpatrick, K. A., Evans, R. H., Ryan, T., & Relph, J. M. (2018). *AVHRR Pathfinder version 5.3 level 3 collated (L3C) global 4km sea surface temperature for 1981-Present.* NOAA National Centers for Environmental Information. Dataset.

Sandeep, K. K., Pant, V., Girishkumar, M. S., & Rao, A. D. (2018). Impact of riverine freshwater forcing on the sea surface salinity simulations in the Indian Ocean. *Journal of Marine Systems*, *185*. https://doi.org/10.1016/j.jmarsys.2018.05.002

Sanil Kumar, V., & Anjali Nair, M. (2015). Inter-annual variations in wave spectral characteristics at a location off the central west coast of India. *Annales Geophysicae*, *33*(2). https://doi.org/10.5194/angeo-33-159-2015

Sarma, V. V. S. S. (2006). The influence of Indian Ocean Dipole (IOD) on biogeochemistry of carbon in the Arabian Sea during 1997-1998. *Journal of Earth System Science*, *115*(4). https://doi.org/10.1007/BF02702872

Schott, F. A., & McCreary, J. P. (2001). The monsoon circulation of the Indian Ocean. In *Progress in Oceanography* (Vol. 51, Issue 1). https://doi.org/10.1016/S0079-6611(01)00083-0

Schott, F. A., Xie, S. P., & McCreary, J. P. (2009). Indian ocean circulation and climate variability. In *Reviews of Geophysics* (Vol. 47, Issue 1). https://doi.org/10.1029/2007RG000245

Seelanki, V., Nigam, T., & Pant, V. (2021). Upper-ocean physical and biological features associated with Hudhud cyclone: A bio-physical modelling study. *Journal of Marine Systems*, *215*. https://doi.org/10.1016/j.jmarsys.2020.103499

Seetaramayya, P., & Master, A. (1984). Observed air-sea interface conditions and a monsoon depression during MONEX-79. *Archives for Meteorology, Geophysics, and Bioclimatology Series A*, *33*(1). https://doi.org/10.1007/BF02265431

Formatted: Font color: Auto

Formatted: Header, Border: Top: (No border), Bottom: (No border), Left: (No border), Right: (No border), Between : (No border), Tab stops: Not at 3.25" + 6.5"

Deleted: Sandeep, S., & Ajayamohan, R. S. (2014). Origin of cold bias over the Arabian Sea in climate models. *Scientific Reports*, *4*. https://doi.org/10.1038/srep06403¶

Formatted: Font color: Auto

Formatted: Font color: Auto

Formatted: Footer, Border: Top: (No border), Bottom: (No border), Left: (No border), Right: (No border), Between : (No border), Tab stops: Not at 3.25" + 6.5"

Shankar, D., Remya, R., Vinayachandran, P. N., Chatterjee, A., & Behera, A. (2016). Inhibition of mixed-layer deepening during winter in the northeastern Arabian Sea by the West India Coastal Current. *Climate Dynamics*, *47*(3–4). https://doi.org/10.1007/s00382-015-2888-3

Shankar, D., & Shetye, S. R. (1997). On the dynamics of the Lakshadweep high and low in the southeastern Arabian Sea. *Journal of Geophysical Research: Oceans*, *102*(C6). https://doi.org/10.1029/97JC00465

Shankar, D., Vinayachandran, P. N., & Unnikrishnan, A. S. (2002). The monsoon currents in the north Indian Ocean. In *Progress in Oceanography* (Vol. 52, Issue 1). https://doi.org/10.1016/S0079-6611(02)00024-1

Shee, A., Sil, S., Gangopadhyay, A., Gawarkiewicz, G., & Ravichandran, M. (2019). Seasonal Evolution of Oceanic Upper Layer Processes in the Northern Bay of Bengal Following a Single Argo Float. *Geophysical Research Letters*, *46*(10). https://doi.org/10.1029/2019GL082078

Shenoi, S. S. C., Shankar, D., & Shetye, S. R. (1999). On the sea surface temperature high in the Lakshadweep Sea before the onset of the southwest monsoon. *Journal of Geophysical Research: Oceans*, *104*(C7). https://doi.org/10.1029/1998jc900080

Skamarock, W. C., & Klemp, J. B. (2008). A time-split nonhydrostatic atmospheric model for weather research and forecasting applications. *Journal of Computational Physics*, *227*(7). https://doi.org/10.1016/j.jcp.2007.01.037

Skamarock WC, et al. (2008). A description of the advanced research WRF version 3, NCAR Tech. Note, NCAR/TN-468+STR. *Natl. Cent. for Atmos. Res. Boulder, Colorado*, *June*.

Song, Y., & Haidvogel, D. (1994). A semi-implicit ocean circulation model using a generalized topography-following coordinate system. *Journal of Computational Physics*, *115*(1). https://doi.org/10.1006/jcph.1994.1189

Sprintall, J., & Tomczak, M. (1992). Evidence of the barrier layer in the surface layer of the tropics. *Journal of Geophysical Research: Oceans*, *97*(C5). https://doi.org/10.1029/92jc00407

Stevenson, J. W., & Niiler, P. P. (1983). Upper Ocean Heat Budget During the Hawaii-to-Tahiti Shuttle Experiment. *Journal of Physical Oceanography*, *13*(10). https://doi.org/10.1175/1520-0485(1983)013<1894:uohbdt>2.0.co;2

Tewari, M., Chen, F., Wang, W., Dudhia, J., LeMone, M. A., Mitchell, K., Ek, M., Gayno, G., Wegiel, J., & Cuenca, R. H. (2004). Implementation and verification of the unified noah land surface model in the WRF model. *Bulletin of the American Meteorological Society*.

Umlauf, L., & Burchard, H. (2003). A generic length-scale equation for geophysical turbulence models. *Journal of Marine Research*, *61*(2). https://doi.org/10.1357/002224003322005087

Vialard, J., Foltz, G. R., McPhaden, M. J., Duvel, J. P., & de Boyer Montégut, C. (2008). Strong Indian Ocean sea surface temperature signals associated with the Madden-Julian Oscillation in late 2007 and early 2008. *Geophysical Research Letters*, *35*(19). https://doi.org/10.1029/2008GL035238

Warner, J. C., Armstrong, B., He, R., & Zambon, J. B. (2010). Development of a Coupled Ocean-Atmosphere-Wave-Sediment Transport (COAWST) Modeling System. *Ocean Modelling*, *35*(3). https://doi.org/10.1016/j.ocemod.2010.07.010

Formatted: Font color: Auto

Formatted: Header, Border: Top: (No border), Bottom: (No border), Left: (No border), Right: (No border), Between : (No border), Tab stops: Not at 3.25" + 6.5"

Moved (insertion) [11]

Formatted: Font color: Auto

Formatted: Font color: Auto

Formatted: Left

Formatted: Font color: Auto

Formatted: Left

Moved up [11]: P.

Deleted: Vinayachandran,

Deleted: N., Shankar, D., Vernekar, S., Sandeep, K. K., Amol, P., Neema, C. P., & Chatterjee, A. (2013). A summer monsoon pump to keep the Bay of Bengal salty. *Geophysical Research Letters*, *40*(9). https://doi.org/10.1002/grl.50274

Formatted: Font color: Auto

Formatted: Font color: Auto

Formatted: Font color: Auto

Formatted: Footer, Border: Top: (No border), Bottom: (No border), Left: (No border), Right: (No border), Between : (No border), Tab stops: Not at 3.25" + 6.5"

Zambon, J. B., He, R., & Warner, J. C. (2014). Investigation of hurricane Ivan using the coupled ocean–atmosphere–wave–sediment transport (COAWST) model. *Ocean Dynamics*, *64*(11). https://doi.org/10.1007/s10236-014-0777-7

Zhang, C., & Wang, Y. (2017). Projected future changes of tropical cyclone activity over the Western North and South Pacific in a 20-km-Mesh regional climate model. *Journal of Climate*, *30*(15). https://doi.org/10.1175/JCLI-D-16-0597.1

Formatted: Font color: Auto

Formatted: Header, Border: Top: (No border), Bottom: (No border), Left: (No border), Right: (No border), Between : (No border), Tab stops: Not at 3.25" + 6.5"

Formatted: Left, Indent: Left: 0.33"

Formatted: Font color: Auto

Formatted: Footer, Border: Top: (No border), Bottom: (No border), Left: (No border), Right: (No border), Between : (No border), Tab stops: Not at 3.25" + 6.5"

Page 1: [1] Formatted **Sankar Prasad Lahiri** **1/18/25 3:08:00 PM**

Font color: Auto

Page 1: [2] Formatted **Sankar Prasad Lahiri** **1/18/25 3:08:00 PM**

Header, Border: Top: (No border), Bottom: (No border), Left: (No border), Right: (No border), Between : (No border), Tab stops: Not at 3.25" + 6.5"

Page 1: [3] Formatted **Sankar Prasad Lahiri** **1/18/25 3:08:00 PM**

Font color: Auto

Page 1: [4] Formatted **Sankar Prasad Lahiri** **1/18/25 3:08:00 PM**

Footer, Border: Top: (No border), Bottom: (No border), Left: (No border), Right: (No border), Between : (No border), Tab stops: Not at 3.25" + 6.5"

Page 1: [5] Style Definition **Sankar Prasad Lahiri** **1/18/25 3:08:00 PM**

Normal (Web)

Page 1: [6] Style Definition **Sankar Prasad Lahiri** **1/18/25 3:08:00 PM**

Comment Text

Page 1: [7] Style Definition **Sankar Prasad Lahiri** **1/18/25 3:08:00 PM**

Revision

Page 1: [8] Style Definition **Sankar Prasad Lahiri** **1/18/25 3:08:00 PM**

Intense Quote

Page 1: [9] Style Definition **Sankar Prasad Lahiri** **1/18/25 3:08:00 PM**

Quote

Page 1: [10] Style Definition **Sankar Prasad Lahiri** **1/18/25 3:08:00 PM**

Subtitle

Page 1: [11] Style Definition **Sankar Prasad Lahiri** **1/18/25 3:08:00 PM**

Title

Page 1: [12] Style Definition **Sankar Prasad Lahiri** **1/18/25 3:08:00 PM**

Footer: Font: (Default) Times New Roman, 10 pt, English (UK), Justified, Tab stops: 3.13", Centered + 6.27", Right + Not at 3.25" + 6.5"

Page 1: [13] Style Definition **Sankar Prasad Lahiri** **1/18/25 3:08:00 PM**

Caption: Font: 10 pt, Not Italic, Font color: Auto, English (UK), Justified

Page 1: [14] Style Definition **Sankar Prasad Lahiri** **1/18/25 3:08:00 PM**

Placeholder Text: Font color: Gray

Page 1: [15] Style Definition **Sankar Prasad Lahiri** **1/18/25 3:08:00 PM**

Hyperlink: Font color: Blue

Page 1: [16] Style Definition **Sankar Prasad Lahiri** **1/18/25 3:08:00 PM**

Header: Font: (Default) Times New Roman, 10 pt, English (UK), Justified, Line spacing: 1.5 lines, Tab stops: 3.15", Centered + 6.3", Right + Not at 3.25" + 6.5"

Page 1: [17] Style Definition **Sankar Prasad Lahiri** **1/18/25 3:08:00 PM**

Heading 9: Outline numbered + Level: 9 + Numbering Style: 1, 2, 3, … + Start at: 1 + Alignment: Left + Aligned at: 0" + Indent at: 1.1"

Page 1: [18] Style Definition **Sankar Prasad Lahiri** **1/18/25 3:08:00 PM**

Heading 8: Outline numbered + Level: 8 + Numbering Style: 1, 2, 3, … + Start at: 1 + Alignment: Left + Aligned at: 0" + Indent at: 1"

Page 1: [19] Style Definition **Sankar Prasad Lahiri** **1/18/25 3:08:00 PM**

Heading 7: Outline numbered + Level: 7 + Numbering Style: 1, 2, 3, … + Start at: 1 + Alignment: Left + Aligned at: 0" + Indent at: 0.9"

Page 1: [20] Style Definition **Sankar Prasad Lahiri** **1/18/25 3:08:00 PM**

Heading 6: Outline numbered + Level: 6 + Numbering Style: 1, 2, 3, … + Start at: 1 + Alignment: Left + Aligned at: 0" + Indent at: 0.8"

Page 1: [21] Style Definition **Sankar Prasad Lahiri** **1/18/25 3:08:00 PM**

Heading 5: Outline numbered + Level: 5 + Numbering Style: 1, 2, 3, … + Start at: 1 + Alignment: Left + Aligned at: 0" + Indent at: 0.7"

Page 1: [22] Style Definition **Sankar Prasad Lahiri** **1/18/25 3:08:00 PM**

Heading 4: Font: (Default) Times New Roman, 10 pt, Bold, Not Italic, Font color: Auto, English (UK), Justified, Space Before: 0 pt, After: 0 pt, Line spacing: 1.5 lines, Outline numbered + Level: 4 + Numbering Style: 1, 2, 3, … + Start at: 1 + Alignmen

Page 1: [23] Style Definition **Sankar Prasad Lahiri** **1/18/25 3:08:00 PM**

Heading 3: Font: 10 pt, Bold, Font color: Auto, English (UK), Justified, Space Before: 12 pt, After: 12 pt, Outline numbered + Level: 3 + Numbering Style: 1, 2, 3, … + Start at: 1 + Alignment: Left + Aligned at: 0" + Indent at: 0.5", Don't keep lines

Page 1: [24] Style Definition **Sankar Prasad Lahiri** **1/18/25 3:08:00 PM**

Heading 2: Font: 10 pt, Bold, Font color: Auto, English (UK), Justified, Space Before: 12 pt, After: 12 pt, Outline numbered + Level: 2 + Numbering Style: 1, 2, 3, … + Start at: 1 + Alignment: Left + Aligned at: 0" + Indent at: 0.4", Don't keep lines

Page 1: [25] Style Definition **Sankar Prasad Lahiri** **1/18/25 3:08:00 PM**

Heading 1: Font: 10 pt, Bold, Font color: Black, English (UK), Kern at 16 pt, Space Before: 24 pt, After: 12 pt, Outline numbered + Level: 1 + Numbering Style: 1, 2, 3, … + Start at: 1 + Alignment: Left + Aligned at: 0" + Indent at: 0.3", Don't keep l

Page 1: [26] Style Definition **Sankar Prasad Lahiri** **1/18/25 3:08:00 PM**

Normal: Font: (Default) Times New Roman, 10 pt, English (UK), Justified, Line spacing: 1.5 lines

Page 1: [27] Formatted **Sankar Prasad Lahiri** **1/18/25 3:08:00 PM**

Font: 17 pt

Page 1: [28] Formatted **Sankar Prasad Lahiri** **1/18/25 3:08:00 PM**

Left

Page 1: [29] Formatted **Sankar Prasad Lahiri** **1/18/25 3:08:00 PM**

Left: 0.65", Right: 0.65", Top: 0.39", Bottom: 0.93", Width: 8.27", Height: 9.45", Header distance from edge: 0", Footer distance from edge: 0.51", From text: 0.16"

Page 1: [30] Formatted **Sankar Prasad Lahiri** **1/18/25 3:08:00 PM**

Font: 12 pt

Page 1: [31] Formatted **Sankar Prasad Lahiri** **1/18/25 3:08:00 PM**

Font: 12 pt

Page 1: [32] Deleted **Sankar Prasad Lahiri** **1/18/25 3:08:00 PM**

Page 1: [33] Formatted **Sankar Prasad Lahiri** **1/18/25 3:08:00 PM**

Left, Indent: First line: 0", Line spacing: single

Page 1: [34] Deleted **Sankar Prasad Lahiri** **1/18/25 3:08:00 PM**

Page 1: [34] Deleted **Sankar Prasad Lahiri** **1/18/25 3:08:00 PM**

Page 1: [35] Formatted **Sankar Prasad Lahiri** **1/18/25 3:08:00 PM**

Font:

Page 1: [35] Formatted **Sankar Prasad Lahiri** **1/18/25 3:08:00 PM**

Font:

Page 1: [36] Formatted **Sankar Prasad Lahiri** **1/18/25 3:08:00 PM**

Font:

Page 1: [37] Formatted **Sankar Prasad Lahiri** **1/18/25 3:08:00 PM**

Font:

Page 1: [38] Formatted **Sankar Prasad Lahiri** **1/18/25 3:08:00 PM**

Font:

Page 1: [39] Formatted **Sankar Prasad Lahiri** **1/18/25 3:08:00 PM**

Font:

Page 1: [40] Deleted **Sankar Prasad Lahiri** **1/18/25 3:08:00 PM**

Page 1: [40] Deleted **Sankar Prasad Lahiri** **1/18/25 3:08:00 PM**

Page 1: [40] Deleted **Sankar Prasad Lahiri** **1/18/25 3:08:00 PM**

Page 1: [40] Deleted **Sankar Prasad Lahiri** **1/18/25 3:08:00 PM**

Page 1: [41] Formatted **Sankar Prasad Lahiri** **1/18/25 3:08:00 PM**

Header, Border: Top: (No border), Bottom: (No border), Left: (No border), Right: (No border), Between : (No border), Tab stops: Not at 3.25" + 6.5"

Page 1: [42] Formatted **Sankar Prasad Lahiri** **1/18/25 3:08:00 PM**

Footer, Border: Top: (No border), Bottom: (No border), Left: (No border), Right: (No border), Between : (No border), Tab stops: Not at 3.25" + 6.5"

Page 5: [43] Deleted **Sankar Prasad Lahiri** **1/18/25 3:08:00 PM**

Page 5: [44] Deleted **Sankar Prasad Lahiri** **1/18/25 3:08:00 PM**

Page 1: [45] Formatted **Sankar Prasad Lahiri** **1/18/25 3:08:00 PM**

Font color: Auto

Page 1: [46] Formatted **Sankar Prasad Lahiri** **1/18/25 3:08:00 PM**

Header, Border: Top: (No border), Bottom: (No border), Left: (No border), Right: (No border), Between : (No border), Tab stops: Not at 3.25" + 6.5"

Page 1: [47] Formatted **Sankar Prasad Lahiri** **1/18/25 3:08:00 PM**

Font color: Auto

Page 1: [48] Formatted **Sankar Prasad Lahiri** **1/18/25 3:08:00 PM**

Footer, Border: Top: (No border), Bottom: (No border), Left: (No border), Right: (No border), Between : (No border), Tab stops: Not at 3.25" + 6.5"

Page 7: [49] Formatted **Sankar Prasad Lahiri** **1/18/25 3:08:00 PM**

Line spacing: single

Page 7: [50] Deleted **Sankar Prasad Lahiri** **1/18/25 3:08:00 PM**

Experiments Name	Ocean model initial & boundary forcing year	Atmospheric forcing year

Page 7: [51] Formatted Table **Sankar Prasad Lahiri**

Formatted Table

Page 7: [52] Deleted **Sankar Prasad Lahiri** **1/18/25 3:08:00 PM**

Page 7: [53] Inserted Cells **Sankar Prasad Lahiri** **1/18/25 3:08:00 PM**

Inserted Cells

Page 7: [54] Formatted **Sankar Prasad Lahiri** **1/18/25 3:08:00 PM**

Left, Line spacing: single

Page 7: [55] Formatted Table **Sankar Prasad Lahiri**

Formatted Table

Page 7: [56] Deleted **Sankar Prasad Lahiri** **1/18/25 3:08:00 PM**

Page 7: [57] Deleted **Sankar Prasad Lahiri** **1/18/25 3:08:00 PM**

Page 7: [58] Inserted Cells **Sankar Prasad Lahiri** **1/18/25 3:08:00 PM**

Inserted Cells

Page 7: [59] Formatted **Sankar Prasad Lahiri** **1/18/25 3:08:00 PM**

Left, Line spacing: single

Page 7: [60] Inserted Cells **Sankar Prasad Lahiri** **1/18/25 3:08:00 PM**

Inserted Cells

Page 7: [61] Formatted **Sankar Prasad Lahiri** **1/18/25 3:08:00 PM**

Left, Line spacing: single

Page 7: [62] Deleted **Sankar Prasad Lahiri** **1/18/25 3:08:00 PM**

Page 7: [63] Deleted **Sankar Prasad Lahiri** **1/18/25 3:08:00 PM**

Page 7: [64] Formatted **Sankar Prasad Lahiri** **1/18/25 3:08:00 PM**

Left, Line spacing: single

Page 7: [65] Deleted **Sankar Prasad Lahiri** **1/18/25 3:08:00 PM**

Page 7: [66] Deleted **Sankar Prasad Lahiri** **1/18/25 3:08:00 PM**

Page 7: [67] Inserted Cells **Sankar Prasad Lahiri** **1/18/25 3:08:00 PM**

Inserted Cells

Page 7: [68] Formatted **Sankar Prasad Lahiri** **1/18/25 3:08:00 PM**

Left, Line spacing: single

Page 7: [69] Change **Sankar Prasad Lahiri** **1/18/25 3:08:00 PM**

Formatted Bullets and Numbering

Page 7: [70] Formatted **Sankar Prasad Lahiri** **1/18/25 3:08:00 PM**

Left, Line spacing: single

Page 7: [71] Deleted **Sankar Prasad Lahiri** **1/18/25 3:08:00 PM**

Page 7: [71] Deleted **Sankar Prasad Lahiri** **1/18/25 3:08:00 PM**

Page 7: [71] Deleted **Sankar Prasad Lahiri** **1/18/25 3:08:00 PM**

Page 7: [71] Deleted **Sankar Prasad Lahiri** **1/18/25 3:08:00 PM**

Page 7: [71] Deleted **Sankar Prasad Lahiri** **1/18/25 3:08:00 PM**

Page 7: [72] Deleted **Sankar Prasad Lahiri** **1/18/25 3:08:00 PM**

Page 7: [72] Deleted **Sankar Prasad Lahiri** **1/18/25 3:08:00 PM**

Page 7: [72] Deleted **Sankar Prasad Lahiri** **1/18/25 3:08:00 PM**

Page 7: [72] Deleted **Sankar Prasad Lahiri** **1/18/25 3:08:00 PM**

Page 7: [72] Deleted **Sankar Prasad Lahiri** **1/18/25 3:08:00 PM**

Page 7: [72] Deleted **Sankar Prasad Lahiri** **1/18/25 3:08:00 PM**

Page 7: [73] Formatted **Sankar Prasad Lahiri** **1/18/25 3:08:00 PM**

Font:

Page 7: [74] Formatted **Sankar Prasad Lahiri** **1/18/25 3:08:00 PM**

Line spacing: single

Page 7: [75] Formatted **Sankar Prasad Lahiri** **1/18/25 3:08:00 PM**

Left, Line spacing: single

Page 1: [76] Formatted **Sankar Prasad Lahiri** **1/18/25 3:08:00 PM**

Footer, Border: Top: (No border), Bottom: (No border), Left: (No border), Right: (No border), Between : (No border), Tab stops: Not at 3.25" + 6.5"

Page 1: [77] Formatted **Sankar Prasad Lahiri** **1/18/25 3:08:00 PM**

Header, Border: Top: (No border), Bottom: (No border), Left: (No border), Right: (No border), Between : (No border), Tab stops: Not at 3.25" + 6.5"

Page 1: [78] Formatted **Sankar Prasad Lahiri** **1/18/25 3:08:00 PM**

Footer, Border: Top: (No border), Bottom: (No border), Left: (No border), Right: (No border), Between : (No border), Tab stops: Not at 3.25" + 6.5"

Page 13: [79] Formatted **Sankar Prasad Lahiri** **1/18/25 3:08:00 PM**

Caption, Left, Space After: 0 pt, Border: Top: (No border), Bottom: (No border), Left: (No border), Right: (No border), Between : (No border)

Page 13: [80] Deleted **Sankar Prasad Lahiri** **1/18/25 3:08:00 PM**

Page 15: [81] Deleted **Sankar Prasad Lahiri** **1/18/25 3:08:00 PM**

Page 15: [82] Deleted **Sankar Prasad Lahiri** **1/18/25 3:08:00 PM**

Page 15: [82] Deleted **Sankar Prasad Lahiri** **1/18/25 3:08:00 PM**

Page 15: [82] Deleted **Sankar Prasad Lahiri** **1/18/25 3:08:00 PM**

Page 15: [82] Deleted **Sankar Prasad Lahiri** **1/18/25 3:08:00 PM**

Page 15: [82] Deleted **Sankar Prasad Lahiri** **1/18/25 3:08:00 PM**

Page 15: [83] Formatted **Sankar Prasad Lahiri** **1/18/25 3:08:00 PM**

Font: Bold

Page 15: [83] Formatted **Sankar Prasad Lahiri** **1/18/25 3:08:00 PM**

Font: Bold

Page 15: [83] Formatted **Sankar Prasad Lahiri** **1/18/25 3:08:00 PM**

Font: Bold

Page 15: [84] Deleted **Sankar Prasad Lahiri** **1/18/25 3:08:00 PM**

Page 15: [84] Deleted **Sankar Prasad Lahiri** **1/18/25 3:08:00 PM**

Page 15: [84] Deleted **Sankar Prasad Lahiri** **1/18/25 3:08:00 PM**

Page 15: [84] Deleted **Sankar Prasad Lahiri** **1/18/25 3:08:00 PM**

Page 15: [85] Deleted **Sankar Prasad Lahiri** **1/18/25 3:08:00 PM**

Page 15: [85] Deleted **Sankar Prasad Lahiri** **1/18/25 3:08:00 PM**

Page 15: [85] Deleted **Sankar Prasad Lahiri** **1/18/25 3:08:00 PM**

Page 15: [85] Deleted **Sankar Prasad Lahiri** **1/18/25 3:08:00 PM**

Page 15: [85] Deleted **Sankar Prasad Lahiri** **1/18/25 3:08:00 PM**

Page 1: [86] Formatted **Sankar Prasad Lahiri** **1/18/25 3:08:00 PM**

Footer, Border: Top: (No border), Bottom: (No border), Left: (No border), Right: (No border), Between : (No border), Tab stops: Not at 3.25" + 6.5"

Page 16: [87] Deleted **Sankar Prasad Lahiri** **1/18/25 3:08:00 PM**

Page 16: [88] Deleted **Sankar Prasad Lahiri** **1/18/25 3:08:00 PM**

Page 16: [89] Deleted **Sankar Prasad Lahiri** **1/18/25 3:08:00 PM**

Page 16: [90] Deleted **Sankar Prasad Lahiri** **1/18/25 3:08:00 PM**

Page 16: [91] Deleted **Sankar Prasad Lahiri** **1/18/25 3:08:00 PM**

Page 16: [92] Deleted **Sankar Prasad Lahiri** **1/18/25 3:08:00 PM**

Page 16: [93] Deleted **Sankar Prasad Lahiri** **1/18/25 3:08:00 PM**

Page 18: [94] Deleted **Sankar Prasad Lahiri** **1/18/25 3:08:00 PM**

Page 1: [95] Formatted **Sankar Prasad Lahiri** **1/18/25 3:08:00 PM**

Footer, Border: Top: (No border), Bottom: (No border), Left: (No border), Right: (No border), Between : (No border), Tab stops: Not at 3.25" + 6.5"

Page 22: [96] Deleted **Sankar Prasad Lahiri** **1/18/25 3:08:00 PM**

Page 24: [97] Deleted **Sankar Prasad Lahiri** **1/18/25 3:08:00 PM**

Page 24: [97] Deleted **Sankar Prasad Lahiri** **1/18/25 3:08:00 PM**

Page 24: [97] Deleted **Sankar Prasad Lahiri** **1/18/25 3:08:00 PM**

Page 24: [97] Deleted **Sankar Prasad Lahiri** **1/18/25 3:08:00 PM**

Page 24: [97] Deleted **Sankar Prasad Lahiri** **1/18/25 3:08:00 PM**

Page 24: [98] Deleted **Sankar Prasad Lahiri** **1/18/25 3:08:00 PM**

Page 24: [98] Deleted **Sankar Prasad Lahiri** **1/18/25 3:08:00 PM**

Page 24: [98] Deleted **Sankar Prasad Lahiri** **1/18/25 3:08:00 PM**

Page 24: [98] Deleted **Sankar Prasad Lahiri** **1/18/25 3:08:00 PM**

Page 24: [99] Formatted **Sankar Prasad Lahiri** **1/18/25 3:08:00 PM**

Font: Not Superscript/ Subscript

Page 24: [99] Formatted **Sankar Prasad Lahiri** **1/18/25 3:08:00 PM**

Font: Not Superscript/ Subscript

Page 24: [100] Deleted **Sankar Prasad Lahiri** **1/18/25 3:08:00 PM**

Page 24: [100] Deleted **Sankar Prasad Lahiri** **1/18/25 3:08:00 PM**

Page 24: [101] Deleted **Sankar Prasad Lahiri** **1/18/25 3:08:00 PM**

Page 25: [102] Deleted **Sankar Prasad Lahiri** **1/18/25 3:08:00 PM**

Page 25: [102] Deleted **Sankar Prasad Lahiri** **1/18/25 3:08:00 PM**

Page 25: [102] Deleted **Sankar Prasad Lahiri** **1/18/25 3:08:00 PM**

Page 25: [102] Deleted **Sankar Prasad Lahiri** **1/18/25 3:08:00 PM**

Page 25: [102] Deleted **Sankar Prasad Lahiri** **1/18/25 3:08:00 PM**

Page 25: [102] Deleted **Sankar Prasad Lahiri** **1/18/25 3:08:00 PM**

Page 25: [103] Deleted **Sankar Prasad Lahiri** **1/18/25 3:08:00 PM**

Page 25: [103] Deleted **Sankar Prasad Lahiri** **1/18/25 3:08:00 PM**

Page 25: [103] Deleted **Sankar Prasad Lahiri** **1/18/25 3:08:00 PM**

Page 25: [103] Deleted **Sankar Prasad Lahiri** **1/18/25 3:08:00 PM**

Page 25: [103] Deleted **Sankar Prasad Lahiri** **1/18/25 3:08:00 PM**

Page 25: [103] Deleted **Sankar Prasad Lahiri** **1/18/25 3:08:00 PM**

Page 25: [103] Deleted **Sankar Prasad Lahiri** **1/18/25 3:08:00 PM**

Page 25: [104] Deleted **Sankar Prasad Lahiri** **1/18/25 3:08:00 PM**

Page 25: [104] Deleted **Sankar Prasad Lahiri** **1/18/25 3:08:00 PM**

Page 25: [104] Deleted **Sankar Prasad Lahiri** **1/18/25 3:08:00 PM**

Page 25: [104] Deleted **Sankar Prasad Lahiri** **1/18/25 3:08:00 PM**

Page 25: [104] Deleted **Sankar Prasad Lahiri** **1/18/25 3:08:00 PM**

Page 25: [104] Deleted **Sankar Prasad Lahiri** **1/18/25 3:08:00 PM**

Page 25: [104] Deleted **Sankar Prasad Lahiri** **1/18/25 3:08:00 PM**

Page 25: [104] Deleted **Sankar Prasad Lahiri** **1/18/25 3:08:00 PM**

Page 25: [104] Deleted **Sankar Prasad Lahiri** **1/18/25 3:08:00 PM**

Page 25: [104] Deleted **Sankar Prasad Lahiri** **1/18/25 3:08:00 PM**

Page 25: [104] Deleted **Sankar Prasad Lahiri** **1/18/25 3:08:00 PM**

Page 25: [104] Deleted **Sankar Prasad Lahiri** **1/18/25 3:08:00 PM**

Page 25: [104] Deleted **Sankar Prasad Lahiri** **1/18/25 3:08:00 PM**

Page 25: [104] Deleted **Sankar Prasad Lahiri** **1/18/25 3:08:00 PM**

Page 25: [104] Deleted **Sankar Prasad Lahiri** **1/18/25 3:08:00 PM**

Page 25: [104] Deleted **Sankar Prasad Lahiri** **1/18/25 3:08:00 PM**

Page 25: [104] Deleted **Sankar Prasad Lahiri** **1/18/25 3:08:00 PM**

Page 25: [105] Deleted **Sankar Prasad Lahiri** **1/18/25 3:08:00 PM**

Page 25: [105] Deleted **Sankar Prasad Lahiri** **1/18/25 3:08:00 PM**

Page 25: [105] Deleted **Sankar Prasad Lahiri** **1/18/25 3:08:00 PM**

Page 25: [105] Deleted **Sankar Prasad Lahiri** **1/18/25 3:08:00 PM**

Page 25: [105] Deleted **Sankar Prasad Lahiri** **1/18/25 3:08:00 PM**

Page 25: [105] Deleted **Sankar Prasad Lahiri** **1/18/25 3:08:00 PM**

Page 25: [105] Deleted **Sankar Prasad Lahiri** **1/18/25 3:08:00 PM**